



**HAL**  
open science

## Identification of real translational and rotational displacements of six-axial shakers with only six measured linear accelerations

Yvon Briend, E. Chatelet, R. Dufour, F. Legrand, S. Baudin

► **To cite this version:**

Yvon Briend, E. Chatelet, R. Dufour, F. Legrand, S. Baudin. Identification of real translational and rotational displacements of six-axial shakers with only six measured linear accelerations. *Mechanical Systems and Signal Processing*, 2021, 154, 10.1016/j.ymssp.2020.107584 . hal-03660112

**HAL Id: hal-03660112**

**<https://hal.science/hal-03660112>**

Submitted on 3 Feb 2023

**HAL** is a multi-disciplinary open access archive for the deposit and dissemination of scientific research documents, whether they are published or not. The documents may come from teaching and research institutions in France or abroad, or from public or private research centers.

L'archive ouverte pluridisciplinaire **HAL**, est destinée au dépôt et à la diffusion de documents scientifiques de niveau recherche, publiés ou non, émanant des établissements d'enseignement et de recherche français ou étrangers, des laboratoires publics ou privés.



Distributed under a Creative Commons Attribution - NonCommercial 4.0 International License

# Identification of real translational and rotational displacements of six-axial shakers with only six measured linear accelerations

Yvon Briend<sup>1,\*</sup>, Eric Chatelet<sup>1</sup>, Régis Dufour<sup>1</sup>, Franck Legrand<sup>1</sup>, Sophie Baudin<sup>2</sup>

---

## Abstract

Qualification tests on the vibrations of on-board equipment depend on the ability of the shaker used to reproduce as precisely as possible the excitation profiles stipulated by standards, given that real operational conditions are generally multi-axial. Using a set of six measured linear accelerations the original method proposed permits determining real six-axial shaker displacements combining three translations and three rotations. Thus, this method, named REDEAT (REal Displacement from Experimental Acceleration with inverse Technique), is useful for introducing these real displacements in the numerical simulation in view of experimentally validating the dynamic behavior model of on-board equipment. Moreover, the REDEAT method evaluates the deviation between real and intended forced displacements. Its principle resides in solving a system of nonlinear time-differential equations expressed, by resorting to numerical integration combining Newmark and Newton-Raphson schemes. In order to overcome the classical divergence issue inherent to the use of numerical integration, data processing tools are employed, consisting of the application of successive high pass filters and window functions. The REDEAT method is applied to a hydraulic 6-DOF shaker equipped with accelerometers and gyroscopes, through a combination of two harmonic rotations and a full 6-DOF random motion. In addition, the influence of the method's parameters and of the six input accelerograms chosen from twelve is investigated.

*Keywords:* 6-DOF shaker, Inverse problem, Nonlinear problem, Multi-axial excitation, Random motion, Experimental technique

---

## 1. INTRODUCTION

In the field of vibratory testing, the qualification of on-board equipment requires taking its real vibration environment into account. Therefore, in order to make the vibration environment as realistic as possible, six degrees-of-freedom (6-DOFs) excitation tests are now preferred to mono-axial tests. The control of the multi-axial shaker must be as reliable as possible. This can be highlighted by the introduction of certain sections on multi-axial excitation in the standards applicable to mechanical equipment qualification (see for instance method 527 of MIL-STD-810G or method 421 of AECTP 400). Indeed, with respect to mono-axial excitation, it initially permits fully representing any arbitrary motion observed under operating conditions. Secondly, it may reduce the duration of the vibration testing, for instance in fatigue life tests or highly accelerated life tests (HALTs), since a multi-axial stress state may be more harmful for the system than a mono-axial one. In this context, the use of multi-axial shakers and research on this topic has tended to increase in the last few years [1–5]. Several solutions are thus being proposed to replace the classical Gough-Stewart platform [6, 7], such as multi-axial tables [8–11] and 6-DOF shakers [12]. Such devices are already able to produce a wide variety of excitation profiles such as sine, random, impact and even the replication of arbitrary signals over wide frequency ranges and amplitudes, with simultaneous translations and rotations. These systems are generally equipped with accelerometers and/or LVDT and driven by targeted accelerations or displacements, considered as references that a closed loop solution tries to reach, using successive and iterative corrections. The real motion measured can be more or less representative of the targeted one, depending on the quality of the correction algorithms, the calibrations of the sensors and their locations, measurement noise, the shaker's performance and linearity, etc. Thus, computing the error between measured and reference accelerations is the first step when qualifying the reliability of the test. Nevertheless, this is generally not enough to figure out the real perturbations producing the remaining error. Indeed, other tools are often required

---

\*Corresponding author: [yvon.briend@insa-lyon.fr](mailto:yvon.briend@insa-lyon.fr)

<sup>1</sup>Univ Lyon, INSA-Lyon, CNRS UMR5259, LaMCoS, F-69621, France

<sup>2</sup>AVNIR Engineering, 62 Boulevard Niels Bohr, 69603 Villeurbanne Cedex, France

to determine the real motion of the shaker, that is to say assessing the time variation in the multi-degrees-of-freedom (MDOFs) of the shaker occurring during the vibration testing. This time information is essential in order to know, for instance, the real amplitudes of the motion, the likely phase between the 6 DOFs and the evolution of the instantaneous axis of rotation.

Several solutions already exist to assess the position, orientation and velocity of a rigid solid, such as the inertial navigation system (INS) [13], also called inertial measurement unit (IMU) [14]. An extensive review of this subject has been published recently by Nilsson and Skog [15]. The sensors used are generally a combination of several accelerometers and gyroscopes in order to obtain the three translations and the three rotations of the structure. Gyroscopes are essential as soon as any rotation occurs but they suffer from several drawbacks such as high cost, high energy consumption, considerable weight, high bias drift, low shock resistance, low dynamic range, and large volume. In this context, many works have been carried out in the last decades to develop IMU using accelerometers only, rather than resorting to gyroscopic sensors. These types of solution are called Gyro-Free or Non-Gyro Inertial Measurement Unit [16, 17]. It is possible to dispense with gyroscopes to obtain the translational accelerations and angular velocities of a rigid-body. Nevertheless this implies that the equations to be solved are necessarily composed with time unknowns and their time-derivatives, namely differential equations. Thus, a classical approach would be to integrate these equations numerically; however, this is troublesome in practice owing to experimental imperfections such as the presence of noise, calibration errors, cross-sensitivity, etc. which generally result in considerable drifts over time when obtaining the displacements. Regarding this point, there are several ways of dealing with these drawbacks. The first and oldest one consists in arranging the accelerometers in a very specific configuration (position and orientation), so as to remove the troublesome terms with time-derivative dependency. This was first proposed in the late 1960s by Schuler *et al* [18], who analyzed several configurations of six and nine accelerometers to obtain the motion of a vehicle, for which some of them were shown to be unstable. Later, the six accelerometer configuration was shown to be unreliable by Padgaonkar *et al* [19] owing to the inherent errors in the measurements. They suggested another specific configuration based on nine accelerometers, which likewise removed the time-derivative dependency in the equations. The applicability of the method was demonstrated with both theoretical and experimental results. More recently, other configurations have been proposed [16]. Nevertheless the aim is always to find the optimal location and orientation of the sensors, which may not be suitable given the singular shapes of certain rigid-bodies.

Another way to treat the differential property of the equations with a more arbitrary sensor configuration is to consider that the unknowns and their time derivative are completely independent algebraic variables. If only the translational accelerations and the angular velocities are to be sought, there are then twelve unknowns to determine [20–23], what will be described in Section 2. In this context, there must be at least twelve mono-axial accelerometers, resulting in an accelerometer array. Nevertheless, a sign ambiguity linked to the quadratic terms in angular velocity always remains. This approach was chosen, for instance, by Cardou *et al* [20] which still resorted to time integration to remove sign indeterminacy for each time step. The feasibility of their method was validated with an experimental test rig using gyroscope data with random and harmonic motions. Likewise, Madgwick *et al* [22] proposed a similar method, tested on a two-axial pendulums instrumented with ten tri-axial accelerometers. The resulting redundancy was then treated by either averaging the accelerometer information or by using the pseudo-inverse method with a least-square solution. Zou *et al* [24] likewise used a redundant array of eight dual-axial accelerometers located in a cylindrical configuration so as to build a 6-DOF sensor. In order to both avoid the need for too many redundant accelerometers and overcome the sign ambiguity of the angular speed, some authors preferred to use Unscented Kalman filters. Among others, Schopp *et al* [21] demonstrated experimentally the efficiency of this method on a 3D rotation table. Later, Edwan *et al* [23] proposed a similar solution which was tested on simulated data with harmonic motions. However, even with these solutions, at least twelve sensors are still needed.

If only six mono-axial accelerometers must be used with a quite arbitrary spatial location, there is no choice left but to perform the numerical integration of the equations of motion. Consequently, it is necessary to know precisely the initial conditions of the system and to overcome the inherent drift obtained with the measurements. Without powerful signal processing tools, this task may quickly appear to be unsuitable owing to the considerable errors accumulated with time, as shown by Giansanti *et al* [25] with a biomechanical application. In their experiments with a vehicle on a track, Onodera *et al* [26] chose to apply a high pass filter after integration combined with an optimal sensor calibration. The relatively good agreement between their method and the gyroscope reference on a 25 s transient motion highlighted the efficiency of the filter. However, it is legitimate to wonder if the latter remains adequate for other types of motion and for sensors with poorer characteristics. Miles [27] used a high-pass filter at each step of the FFT-based integration process to remove the divergence. This method permitted obtaining the angular displacements in the transient excitation of an offshore supply vessel and a semisubmersible platform at a scale of 1:40. The results were validated with an optical tracking system composed of five cameras. Nevertheless, the translational DOFs were not assessed, and no information was available

regarding the possible side effects associated with successive high pass filters.

The aim of the present paper is to propose a new technique to accurately determine the complete rotational and translational displacements of any 6-DOF shaker, without inertial or kinetic knowledge. This method, called REDEAT (REal Displacement from Experimental Acceleration with inverse Technique), first permits having the most reliable base displacements that can be introduced into the model for predicting the dynamic behavior of on-board structures. Thus, the numerical and experimental correlation can be enhanced. Secondly, it can also help to improve the shaker driving process, for instance, thanks to better knowledge of the actual position of the instantaneous axis of rotation. Since most of these devices are driven in closed-loop mode using accelerometers data as feedback, it is expedient to use the same accelerometers to obtain the measured motion, instead of resorting to other expensive and limited instrumentation such as gyroscopes or additional accelerometers. For this reason, it was decided to use acceleration data only. In contrast with the previous works cited above, the solutions are given in terms of six displacements rather than three translational accelerations and three angular velocities, using only six accelerograms corresponding to sensors in an arbitrary spatial configuration, and without the use of Kalman filters. The problem is solved by numerical integration combined with efficient data processing tools that consist in applying successive high-pass filters and window functions defined through three parameters. This solution is tested on a hydraulic shaker with multi-axial harmonic and random motions, and validated through additional instrumentation such as other accelerometers and gyroscopes. Emphasis is placed on pure rotational motion, the importance of the filtering process, the computational cost and the sensor configuration.

## 2. THEORY

### 2.1. Kinematics of a 6-DOF rigid-body

Defining the motion of a rigid-body requires two frames of reference. The first one  $R_0(O_0, \vec{X}_0, \vec{Y}_0, \vec{Z}_0)$  is considered to be the Galilean frame and the second one  $R(O, \vec{x}, \vec{y}, \vec{z})$  the moving frame which is fixed to the shaker. The full rotational motion of  $R$  with respect to  $R_0$  can be defined by the Euler angles, so that  $R$  is obtained through three following successive rotations: the precession angle  $\alpha_1$  around  $\vec{Z}_0$  creating a first intermediary frame  $R_1(O_0, \vec{X}_1, \vec{Y}_1, \vec{Z}_1)$  with  $\vec{Z}_1 = \vec{Z}_0$ , the nutation angle  $\alpha_2$  around  $\vec{X}_1$  creating a second intermediary frame  $R_2(O_0, \vec{X}_2, \vec{Y}_2, \vec{Z}_2)$  with  $\vec{X}_1 = \vec{X}_2$ , the intrinsic rotation angle  $\alpha_3$  around  $\vec{Y}_2$  creating the frame  $R$  with  $\vec{Y}_2 = \vec{y}$ , as illustrated in Fig. 1.

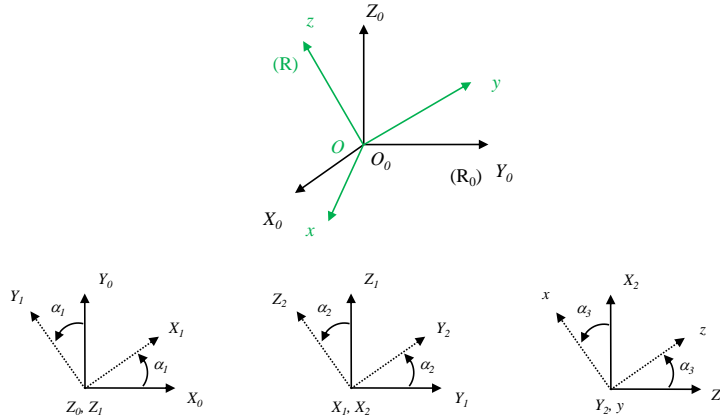


Figure 1: Definition of the two frames of reference by using the Euler angles

In the same way, these angles are implicitly time-dependent. At this point, it is possible to link the set of vectors from one frame of reference with respect to the other one with the following orthogonal transformation:

$$\begin{pmatrix} \vec{X}_0 \\ \vec{Y}_0 \\ \vec{Z}_0 \end{pmatrix} = [P_{R_0 \rightarrow R}] \begin{pmatrix} \vec{x} \\ \vec{y} \\ \vec{z} \end{pmatrix} \quad (1)$$

with

$$[P_{R_0 \rightarrow R}] = \begin{bmatrix} \cos(\alpha_1) \cos(\alpha_3) - \sin(\alpha_1) \sin(\alpha_2) \sin(\alpha_3) & -\sin(\alpha_1) \cos(\alpha_2) & \cos(\alpha_1) \sin(\alpha_3) + \sin(\alpha_1) \sin(\alpha_2) \cos(\alpha_3) \\ \sin(\alpha_1) \cos(\alpha_3) + \cos(\alpha_1) \sin(\alpha_2) \sin(\alpha_3) & \cos(\alpha_1) \cos(\alpha_2) & \sin(\alpha_1) \sin(\alpha_3) - \cos(\alpha_1) \sin(\alpha_2) \cos(\alpha_3) \\ -\cos(\alpha_2) \sin(\alpha_3) & \sin(\alpha_2) & \cos(\alpha_2) \cos(\alpha_3) \end{bmatrix} \quad (2)$$

an orthogonal rotation matrix such that  $[P_{R_0 \rightarrow R}]^{-1} = [P_{R_0 \rightarrow R}]^T = [P_{R \rightarrow R_0}]$ .

The instantaneous angular velocity vector  $\vec{\Omega}_R^{R_0}$ , characteristic of the rotation of the moving frame  $R$  with respect to  $R_0$ , can be defined using the three Euler angles mentioned above according to:

$$\vec{\Omega}_R^{R_0} = \dot{\alpha}_1 \vec{Z}_0 + \dot{\alpha}_2 \vec{X}_1 + \dot{\alpha}_3 \vec{Y}_2 \quad (3)$$

By performing a scalar dot product between the vectors of  $R$  and the vectors  $\vec{Z}_0$ ,  $\vec{X}_1$  and  $\vec{Y}_2$ ,  $\vec{\Omega}_R^{R_0}$  can be expressed in  $R$  such that:

$$\vec{\Omega}_R^{R_0} = \begin{Bmatrix} \omega_x^0 \\ \omega_y^0 \\ \omega_z^0 \end{Bmatrix}_R \quad (4)$$

where

$$\omega_x^0 = -\dot{\alpha}_1 \cos(\alpha_2) \sin(\alpha_3) + \dot{\alpha}_2 \cos(\alpha_3) \quad (5a)$$

$$\omega_y^0 = \dot{\alpha}_1 \sin(\alpha_2) + \dot{\alpha}_3 \quad (5b)$$

$$\omega_z^0 = \dot{\alpha}_1 \cos(\alpha_2) \cos(\alpha_3) + \dot{\alpha}_2 \sin(\alpha_3) \quad (5c)$$

are respectively the components of the instantaneous angular velocity vector in  $\vec{x}$ ,  $\vec{y}$  and  $\vec{z}$ , which are given directly by a gyroscope that would be fixed in  $R$ . In this sense, they will be used instead of  $(\dot{\alpha}_1, \dot{\alpha}_2, \dot{\alpha}_3)$  to validate the REDEAT method proposed for the rotation problem.

The translational motion of  $R$  with respect to  $R_0$  is defined through the motion of the origin  $O$  of  $R$  in  $R_0$  by the vector  $\overrightarrow{O_0 O}$  such that:

$$\overrightarrow{O_0 O} = \begin{Bmatrix} X_0 \\ Y_0 \\ Z_0 \end{Bmatrix}_{R_0} \quad (6)$$

where  $X_0$ ,  $Y_0$  and  $Z_0$  are the displacements of  $O$  along the axes  $\vec{X}_0$ ,  $\vec{Y}_0$  and  $\vec{Z}_0$  respectively.

By using this specific kinematics, it is now possible to fully describe any 6-DOF motion taking place. There are two ways of achieving this: the first one consists in decomposing the motion of any point into a sum of a translation motion and a rotation motion with a constant radius; the second one consists in assuming a pure rotational motion with a time-varying radius related to the instantaneous axis of rotation, that goes to infinity if there are only translations. The technique proposed uses the former option which is the most intuitive and straightforward one. To this end, let the in-plane example of Fig. 2 be considered, consisting of a 2D-translation and a 1D-rotation of an arbitrary point  $A$  fixed in  $R$ , defined by the constant coordinates  $(x_A, y_A, z_A)$  in  $R$ . The rotation acts at an angle  $\alpha_1$  and a constant radius  $C$ , around the axis  $\vec{Z}_0$  of  $R_0$  passing through  $O$  so that  $\overrightarrow{OA} = C\vec{x}$ . Meanwhile, the motion of  $O$  is free in  $R_0$  and defined by the vector  $\overrightarrow{O_0 O}$ . The displacement of  $A$  in  $R_0$  can be found as:

$$\overrightarrow{O_0 A} = \overrightarrow{O_0 O} + \overrightarrow{OA} = \begin{Bmatrix} X_0 \\ Y_0 \\ Z_0 \end{Bmatrix}_{R_0} + \begin{Bmatrix} x_A \\ y_A \\ z_A \end{Bmatrix}_R = \begin{Bmatrix} X_0 \\ Y_0 \\ Z_0 \end{Bmatrix}_{R_0} + [P_{R_0 \rightarrow R}] \begin{Bmatrix} x_A \\ y_A \\ z_A \end{Bmatrix} \quad (7)$$

where, for this example,  $X_A = X_0 + C \cos(\alpha_1)$ ,  $Y_A = Y_0 + C \sin(\alpha_1)$  and  $Z_A = Z_0 = 0$  are the coordinates of  $A$  in  $R_0$ .

In this way, the 6 DOFs of any point fixed to the shaker can be defined as the three translations  $X_0$ ,  $Y_0$  and  $Z_0$  along the axes of  $R_0$  and the three rotations  $(\alpha_1, \alpha_2, \alpha_3)$  around the axes  $(\vec{Z}_0, \vec{X}_1, \vec{Y}_2)$  all passing by the origin  $O$  of  $R$ . In the case of simultaneous translations and rotations, the instantaneous axis of rotation, directed by the vector  $\vec{\Omega}_R^{R_0}$  of Eq. (3), no longer passes through  $O$  but rather on a varying point that can be found only by assessing the linear velocities of several points fixed in  $R$ .

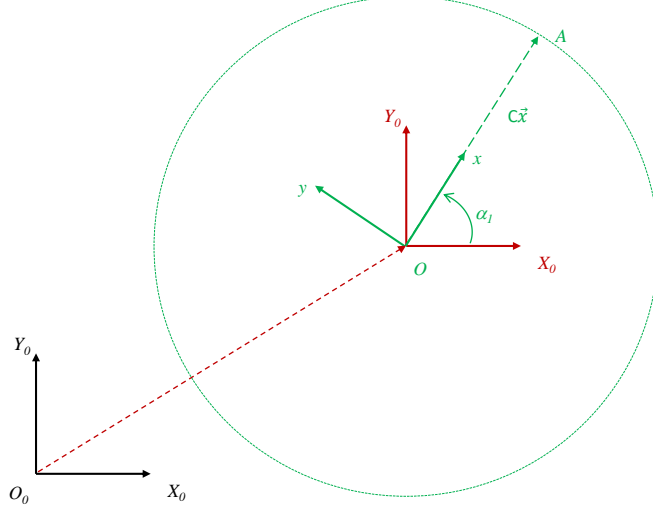


Figure 2: In-plane motion of a point  $A$  with a rotation of angle  $\alpha_1$  and radius  $C$  and a translation of  $X_0$  and  $Y_0$

## 2.2. Direct and inverse problem

As stated in Section 1, 6-DOF shakers can be driven by means of accelerometric data used as feedback within a closed loop correction algorithm. Hence, a possible approach to create a targeted multi-axial motion of the shaker is to define the time variations of the 6 DOFs detailed in Section 2.1 when the moving frame  $R$  is fixed to the shaker, and then to compute the targeted accelerations that must be detected by the accelerometers fixed to the system. These accelerations may be used afterwards as the references to be reached by the closed loop algorithm. This will be called the direct problem as represented in Fig. 3 where  $\gamma_i$  stand for these targeted accelerations.

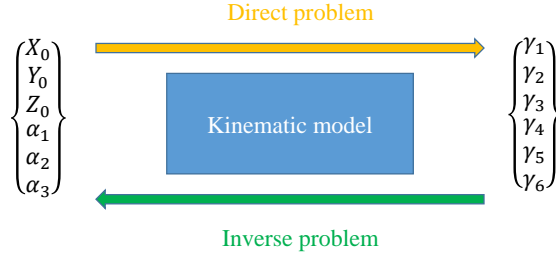


Figure 3: Principle of the direct and inverse problems

In order to obtain these targeted accelerations, the first step consists in deriving the position of the corresponding accelerometers twice with respect to time in relation to the Galilean frame of reference  $R_0$ . Let an arbitrary mono-axial accelerometer located in  $A$  in Fig. 2 with the coordinates  $(x_A, y_A, z_A)$  in  $R$  be considered as an illustration. Its position with respect to  $R_0$ , given by Eq. (7), is then derived twice with respect to time. The resulting acceleration must be expressed back in the moving frame  $R$  since the accelerometer and its direction are fixed in  $R$ . Consequently, the targeted linear acceleration  $\vec{\gamma}$  detected by the accelerometer turns out as:

$$\vec{\gamma} = [P_{R_0 \rightarrow R}]^T \left( \begin{matrix} \ddot{X}_0 \\ \ddot{Y}_0 \\ \ddot{Z}_0 \end{matrix} \right)_{R_0} + [P_{R_0 \rightarrow R}] \begin{matrix} x_A \\ y_A \\ z_A \end{matrix} + \vec{g} \quad (8)$$

where the notation  $(\ddot{\cdot})$  denotes twice the differentiation with time. Vector  $\vec{g} = -g\vec{Z}_0$  is the gravitational acceleration which has been added since it may contribute to the actual acceleration detected by the accelerometer if the latter is designed for

low frequency values or in the case of large rotations. The acceleration of Eq. (8) is actually composed of three components in  $(\vec{x}, \vec{y}, \vec{z})$  while the sensing direction of the sensor is only directed along one of these axes or along a fixed combination of them. Hence, only one row of Eq. (8) or a linear combination of the three rows is used for a mono-axial accelerometer. The same principle can be applied for the other sensors and the resulting six accelerations are finally used as references for the closed-loop algorithm working for instance in time waveform replication.

In practice, the real motion will not be perfectly similar to the targeted one. This may originate from several sources of errors such as the sensors (cross sensitivity, imperfect calibration, measurement noise), the shaker (nonlinear responses, likely elastic deformation within the operational frequency band, displacement limitations) and the closed-loop algorithm (imperfect characterization of the shaker's transfer functions, bad tolerances or poor corrections for the convergence). In order to evaluate the differences between the targeted and the real motions, it is relevant to perform what is called the inverse problem shown in Fig. 3 the aim of which is to use the measured accelerations to obtain the real time variation of the 6 DOFs of the system. This is done by using Eq. (8) once again for which the acceleration  $\vec{\gamma}$  is now given data of the problem, namely the experimental acceleration, and in which the 6 DOFs are the unknowns. If no link is made between the variables and their time derivatives, this equation will contain twelve unknowns:  $(\ddot{X}_0, \ddot{Y}_0, \ddot{Z}_0)$  the translational accelerations and  $(\alpha_1, \alpha_2, \alpha_3, \dot{\alpha}_1, \dot{\alpha}_2, \dot{\alpha}_3, \ddot{\alpha}_1, \ddot{\alpha}_2, \ddot{\alpha}_3)$  the angular displacements, velocities and accelerations present in the matrices and  $[P_{R_0 \rightarrow R}]$  and  $[\dot{P}_{R_0 \rightarrow R}]$ . The latter matrix will not be explicitly described here owing to its great complexity. However, it contains trigonometric functions of the angular displacements multiplying either quadratic terms in angular velocities or linear terms in angular accelerations, which make the equation nonlinear. On the other hand, if the angular DOFs are considered related, the problem is reduced to six unknowns which may be either  $(\ddot{X}_0, \ddot{Y}_0, \ddot{Z}_0, \ddot{\alpha}_1, \ddot{\alpha}_2, \ddot{\alpha}_3)$  or  $(\ddot{X}_0, \ddot{Y}_0, \ddot{Z}_0, \alpha_1, \alpha_2, \alpha_3)$  depending on the user's preference. In the present paper, the second choice is retained to simplify the expression of the discretized problem detailed in the following section. Therefore, by using the information of six sensors, the inverse problem consists in solving the following differential nonlinear system of equation:

$$f_i(\ddot{X}_0, \ddot{Y}_0, \ddot{Z}_0, \alpha_1, \alpha_2, \alpha_3) = \gamma_i \quad i \in 1..6 \quad (9)$$

where  $\gamma_i = \vec{\gamma}_i \cdot \vec{n}_i$  with  $\vec{\gamma}_i$  the 3D acceleration vector of the point where the accelerometer  $i$  is located,  $\vec{n}_i$  the direction of the accelerometer  $i$  and “ $\cdot$ ” the dot scalar product.

### 2.3. Solving of the inverse problem - time integration loop

By looking at Eq. (8), it can be seen that the translational part does not depend on the accelerometer. Thus, a good strategy is to uncouple the problem by removing the translational variables. This will be denoted as the rotation problem and can be achieved by subtracting the accelerations of two accelerometers  $i$  and  $j$  having the same direction  $\vec{n}_i = \vec{n}_j$  and located at two different positions. Then, using Eq. (8), we obtain:

$$\left( [P_{R_0 \rightarrow R}]^T [\dot{P}_{R_0 \rightarrow R}] \vec{U}_{i,j} \right) \cdot \vec{n}_i = \gamma_i - \gamma_j \quad (10)$$

where

$$\vec{U}_{i,j} = \begin{Bmatrix} x_{A_i} - x_{A_j} \\ y_{A_i} - y_{A_j} \\ z_{A_i} - z_{A_j} \end{Bmatrix} \quad (11)$$

is a time-independent vector that depends only on the choice of the sensors and their location. By doing this, both translational and gravitational accelerations are canceled. The next step consists in determining the angular variables. Therefore, numerical integration is needed and the well-established Newmark approximation with constant-average-acceleration [28] is used here to discretize Eq. (10). However, for the sake of simplicity, this approximation is applied directly to the matrix  $[\ddot{P}_{R_0 \rightarrow R}]$  instead of the angular accelerations  $(\ddot{\alpha}_1, \ddot{\alpha}_2, \ddot{\alpha}_3)$  and angular velocities  $(\dot{\alpha}_1, \dot{\alpha}_2, \dot{\alpha}_3)$  present in this matrix. Thus, at the next unknown time iteration  $t + \Delta t$  where  $\Delta t$  is the time step, the matrix is related to the previous known time iteration  $t$  by:

$$[\ddot{P}_{R_0 \rightarrow R}]_{t+\Delta t} = a_0 ([P_{R_0 \rightarrow R}]_{t+\Delta t} - [P_{R_0 \rightarrow R}]_t) - a_2 [\dot{P}_{R_0 \rightarrow R}]_t - a_3 [\ddot{P}_{R_0 \rightarrow R}]_t \quad (12)$$

with  $a_0 = \frac{1}{\alpha(\Delta t)^2}$ ,  $a_2 = \frac{1}{\alpha \Delta t}$ ,  $a_3 = \frac{1}{2\alpha} - 1$  and  $\alpha = 0.25$ . Then, by substituting the Newmark approximation of Eq. (12) in Eq. (10) defined at time iteration  $t + \Delta t$ , we obtain:

$$\left( [P_{R_0 \rightarrow R}]_{t+\Delta t}^T \left( a_0 [P_{R_0 \rightarrow R}]_t + a_2 [\dot{P}_{R_0 \rightarrow R}]_t + a_3 [\ddot{P}_{R_0 \rightarrow R}]_t \right) \vec{U}_{i,j} \right) \cdot \vec{n}_i = a_0 \vec{U}_{i,j} \cdot \vec{n}_i - (\gamma_{i,t+\Delta t} - \gamma_{j,t+\Delta t}) \quad (13)$$

This equation is nonlinear in  $(\alpha_{1,t+\Delta t}, \alpha_{2,t+\Delta t}, \alpha_{3,t+\Delta t})$  that compose the matrix  $[P_{R_0 \rightarrow R}]_{t+\Delta t}^T$ , because of the trigonometric functions (see Eq. (2)). In the case of small displacements, the matrix could eventually be linearized to obtain a linear problem. However, for the sake of completeness, the general case with arbitrary displacements, and hence the nonlinear problem, is addressed in this paper. The numerical scheme used to solve it is the Newton-Raphson scheme [28]. Thus, from Eq. (13) the following residual  $r_{i,j} = r_{i,j}(\alpha_{1,t+\Delta t}, \alpha_{2,t+\Delta t}, \alpha_{3,t+\Delta t})$  is built such that:

$$r_{i,j} = \left( [P_{R_0 \rightarrow R}]_{t+\Delta t}^T \left( a_0 [P_{R_0 \rightarrow R}]_t + a_2 [\dot{P}_{R_0 \rightarrow R}]_t + a_3 [\ddot{P}_{R_0 \rightarrow R}]_t \right) \vec{U}_{i,j} \right) \cdot \vec{n}_i - a_0 \vec{U}_{i,j} \cdot \vec{n}_i + (\gamma_{i,t+\Delta t} - \gamma_{j,t+\Delta t}) \quad (14)$$

with the subscripts  $(i, j)$  that denote the acceleration  $\gamma_i$  and  $\gamma_j$  of the mono-axial accelerometers  $A_i$  and  $A_j$ , respectively. Since there are three unknowns, three equations are necessary. Consequently, two more sets of two accelerometers must be used like for Eq. (14), each set with one specific direction, so as to obtain the following residual vector:

$$\{R\} = \begin{Bmatrix} r_{i_1, j_1} \\ r_{i_2, j_2} \\ r_{i_3, j_3} \end{Bmatrix} \quad (15)$$

which must be canceled to find the solution of the nonlinear problem. The subscripts  $(i_1, j_1, i_2, j_2, i_3, j_3)$  are integers used to choose among the accelerograms available. This choice is based on how to make the problem solvable. For instance,  $(i, j)$  must correspond to two accelerations in the same direction, but for different positions (i.e.  $i \neq j$ ). Moreover, an optimal configuration of accelerometer positions will facilitate enhancing both the condition number of the matrix to be inverted and the accuracy of the results. This is analyzed in more detail in Section 4.2.

The next step of the Newton-Raphson scheme is to compute the tangent matrix  $[T]$  by deriving the residual vector  $\{R\}$  of Eq. (15) with respect to each of the angular displacements at unknown time iteration  $t + \Delta t$  such that:

$$[T] = \left[ \frac{\partial R}{\partial \alpha_{t+\Delta t}} \right] \quad (16)$$

and to iterate over  $r$  with:

$$\begin{Bmatrix} \alpha_1 \\ \alpha_2 \\ \alpha_3 \end{Bmatrix}_{t+\Delta t}^{(r+1)} = \begin{Bmatrix} \alpha_1 \\ \alpha_2 \\ \alpha_3 \end{Bmatrix}_{t+\Delta t}^{(r)} - \left( [T]_{t+\Delta t}^{(r)} \right)^{-1} \{R\}_{t+\Delta t}^{(r)} \quad (17)$$

where the superscript  $r$  is the Newton-Raphson iteration parameter. Once the convergence is obtained, the angular accelerations and velocities can be computed afterwards at time  $t + \Delta t$  by using the following Newmark approximations:

$$\begin{Bmatrix} \ddot{\alpha}_1 \\ \ddot{\alpha}_2 \\ \ddot{\alpha}_3 \end{Bmatrix}_{t+\Delta t} = a_0 \left( \begin{Bmatrix} \alpha_1 \\ \alpha_2 \\ \alpha_3 \end{Bmatrix}_{t+\Delta t} - \begin{Bmatrix} \alpha_1 \\ \alpha_2 \\ \alpha_3 \end{Bmatrix}_t \right) - a_2 \begin{Bmatrix} \dot{\alpha}_1 \\ \dot{\alpha}_2 \\ \dot{\alpha}_3 \end{Bmatrix}_t - a_3 \begin{Bmatrix} \ddot{\alpha}_1 \\ \ddot{\alpha}_2 \\ \ddot{\alpha}_3 \end{Bmatrix}_t \quad (18a)$$

$$\begin{Bmatrix} \dot{\alpha}_1 \\ \dot{\alpha}_2 \\ \dot{\alpha}_3 \end{Bmatrix}_{t+\Delta t} = \begin{Bmatrix} \dot{\alpha}_1 \\ \dot{\alpha}_2 \\ \dot{\alpha}_3 \end{Bmatrix}_t + a_6 \begin{Bmatrix} \ddot{\alpha}_1 \\ \ddot{\alpha}_2 \\ \ddot{\alpha}_3 \end{Bmatrix}_{t+\Delta t} + a_7 \begin{Bmatrix} \ddot{\alpha}_1 \\ \ddot{\alpha}_2 \\ \ddot{\alpha}_3 \end{Bmatrix}_t \quad (18b)$$

with  $a_6 = (1 - \delta)\Delta t$ ,  $a_7 = \delta\Delta t$  and  $\delta = 0.5$  [28].

Without loss of generality, the first iteration  $r = 1$  can be initialized with the solution obtained at the previous iteration of time  $t$ . Regarding the Newmark process, the initial conditions must be as reliable as possible to avoid divergence of the algorithm. A simple idea consists in starting the acquisition when the system is at rest where all the accelerations, velocities and displacements are nil. In this way, the Newmark scheme is initialized with nil conditions. Provided noise in the measurements is sufficiently low, these initial conditions are the most reliable ones.

Once the angular displacements, velocities and accelerations are calculated at each time step, the translational variables can be computed; this will be denoted the translation problem. To this end, the translational accelerations can be isolated from Eq. (8) so that:

$$\begin{Bmatrix} \ddot{X}_0 \\ \ddot{Y}_0 \\ \ddot{Z}_0 \end{Bmatrix}_{R_0} = [P_{R_0 \rightarrow R}] \vec{\gamma}_i - [\ddot{P}_{R_0 \rightarrow R}] \begin{Bmatrix} x_{A_i} \\ y_{A_i} \\ z_{A_i} \end{Bmatrix} - \vec{g} \quad (19)$$

It can be seen in this last equation that the accelerations in the three directions must be known at the same location. This may be obtained with a tri-axial sensor or with three mono-axial sensors. Some of these accelerations may have already been used for the previous rotation problem, in order not to exceed the maximum number of six accelerograms to be used. It should be recalled here that if the sensors cannot capture low frequencies or static components and if the angular displacements remain small it may be necessary to cancel the gravitational acceleration in Eq. (19).

Finally, the translational displacements  $(X_0, Y_0, Z_0)$  remain to be computed by a double integration of the translational accelerations  $(\ddot{X}_0, \ddot{Y}_0, \ddot{Z}_0)$ , which can be done for instance with another Newmark approximation, as in Eqs. (18).

#### 2.4. Data processing for convergence requirement

As stated in Section 1, the main issue associated with the use of numerical time integration to obtain the complete motion of the system is the likely divergences that occur owing to several reasons such as the noise in the measurements, the calibration sensor bias, the uncertainties of the sensor locations, the imperfect knowledge of the initial conditions, etc. In some rare cases, divergence behavior may be canceled after the completion of the steps described in Section 2.3. This is the case when there are static components in the acceleration or non-zero mean, leading to a quadratic time divergence of the type  $x(t) + C_2t^2 + C_1t$  where  $C_2$  and  $C_1$  are arbitrary constants and  $x(t)$  is the real time variation of one of the 6 DOFs. By applying a high-pass filter, the spurious part  $C_2t^2 + C_1t$  can be easily removed and  $x(t)$  can be isolated provided the latter does not contain any frequency below the cut-off frequency of the filter. Unfortunately, in most cases, this first divergence when acting with the rotation DOFs quickly induces a second divergence in the variation of  $x(t)$  that cannot be corrected afterwards. That is why the high-pass filter has to be applied earlier and several times within the time loop of the numerical integration described in Section 2.3 for each angular DOF. A radical solution is to apply it at each time step of the time integration process as described by Miles [27]. However, this author did not mention the likely side effects related to the filtering and how to deal with them. Furthermore, successive filtering may not only result in drastically increasing the computational cost, but it can also greatly reduce or increase the original signal if the same parts of the signal are filtered several times.

The alternative proposed in the present paper is to apply high-pass filters with cut-off frequency  $f_c$ , which is the first parameter of the REDEAT method, however not for each time step but rather at every  $t_0$  where  $t_0$  is the second parameter. The latter is a time duration that will depend on the spectral content of the signal. This is performed in combination with the use of a sine window function defined by the third parameter  $t_1$ , at the beginning and the end of the DOF time-variation already computed, in order to remove likely side effects of the filter.

To better illustrate this approach, let the following example be addressed. A mono-axial rotation of  $\alpha_2 = A_2 \cos(2\pi 10t)$  with  $A_2 = 1^\circ$  is imposed on the system, regardless of the center of rotation. This sinusoid is modified at the beginning of the signal so that it slowly reaches its final full amplitude and consequently it has a smooth transition from  $0^\circ$  to  $1^\circ$ . The parameter  $t_0$  is set arbitrarily to 0.5 s. In order to determine the real motion, the algorithm described in Section 2.3 is employed and stopped at an arbitrary instant of time  $t^* = 5.615$  s. As mentioned above, an undesired divergence in the original signal occurs since filtering has not been applied, that is to say since  $t = t^* - t_0 = 5.115$  s, see Fig. 4a. The first step of the data processing consists in multiplying the original signal  $\alpha_2(t)$  by a window function  $W(t)$  of half-sine type and variable length defined in the following way:

$$W(t) = W_1(t).W_2(t) \tag{20a}$$

$$W_1(t) = \begin{cases} \frac{1}{2} \left( 1 + \cos \left( \pi \frac{t}{t_1} + \pi \right) \right) & \forall t \in [0; t_1] \\ 1 & \forall t > t_1 \end{cases} \tag{20b}$$

$$W_2(t) = \begin{cases} 1 & \forall t \in [0; t^* - t_1[ \\ \frac{1}{2} \left( 1 + \cos \left( \pi \frac{t - (t^* - t_1)}{t_1} \right) \right) & \forall t \in [t^* - t_1; t^*] \\ 0 & \forall t > t^* \end{cases} \tag{20c}$$

where  $t_1$  is likewise a time duration that must respect  $0 < t_1 < t_0$ . In this example,  $t_1$  is set to 0.2 s as seen in Fig. 4b. Next, a high-pass filter of cut-off frequency  $f_c$ , 4 Hz in this example, is applied to the resulting signal to obtain the modified signal of Fig. 4c where the divergence has been removed. Owing to the windowing, only the interval of time  $t \in [t^* - t_0; t^* - t_1]$  must be kept. Then, the time integration loop must restart at the time instant  $t = t^* - t_1$  (here 5.415 s), until the next time instant  $t = t^* - t_1 + t_0$  distant from  $t_0$  where the data processing will once again be applied, etc. By going backward in time, some parts of the signal must be recomputed several times. This consequently increases the time

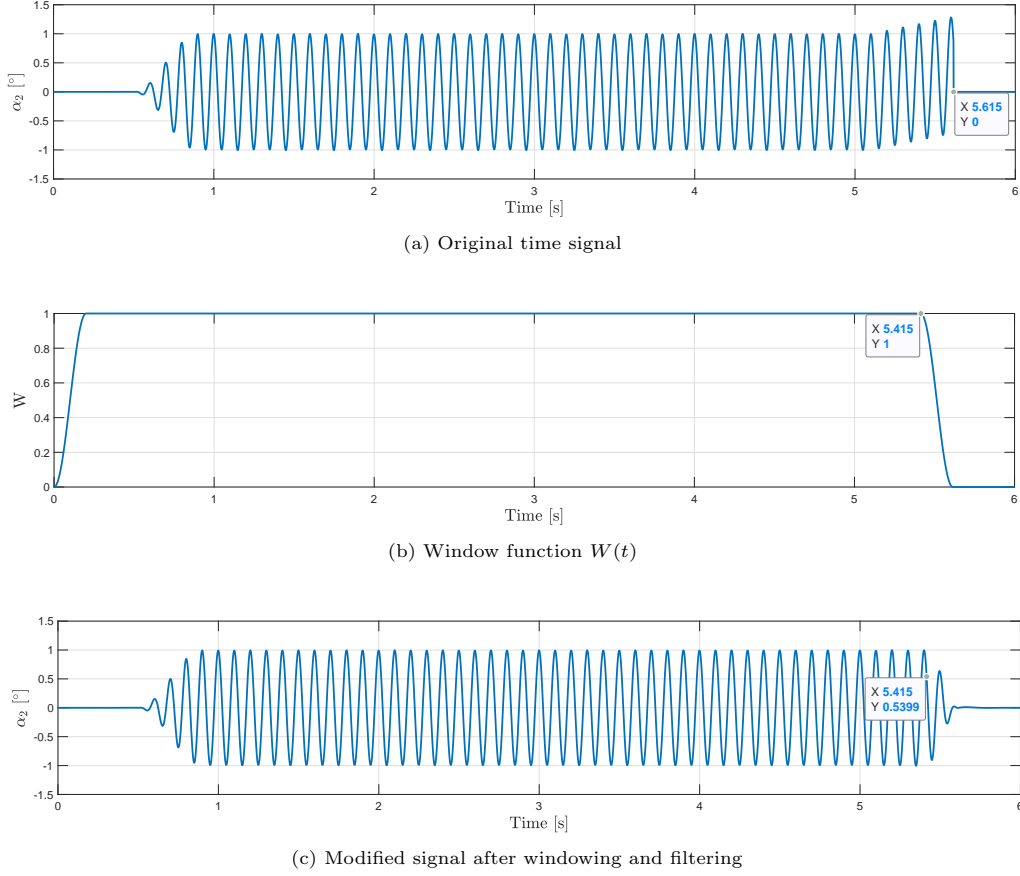


Figure 4: Data processing within the time integration loop

cost. Nevertheless, it permits having enough new data to be filtered and for every time instant in the signal to be filtered only once. The purpose of the window function is for the signal to present the same value at its two extremities and thus reduce the likely side effects created by the further filtering process, especially when using a very low cut-off frequency. Therefore, the signal tends to nil values before applying filtering even with the accumulation of errors due, for instance, to poor knowledge of the initial conditions or measurement noise. Because of this window, static non-zero components in the rotations must be avoided, for instance by defining the orientation of the Galilean frame  $R_0$  to be same as  $R$  at rest.

By construction, the algorithm will stop performing this data processing at each time instant  $t^* = t^*(p) = p(t_0 - t_1) + t_0$  where  $p$  is a natural integer starting at 0. Depending on the choice of the parameter  $t_0$  and  $t_1$ , it is possible that this window  $W$  does not reach unitary value for the first iteration of  $p$ . This does not happen only if  $t_1 > t^* - t_1$ , i.e. for any  $p > p_s = \left\lceil \frac{2t_1 - t_0}{t_0 - t_1} \right\rceil$ . Moreover, since the results of the inverse problem are kept only in  $t \in [t^* - t_0; t^* - t_1]$ , it is recommended to start the measurements at least  $t^*(p_s) - t_0 = p_s(t_0 - t_1)$  s before the motion of the system actually starts. Firstly, this ensures that no essential accelerometric information is lost and secondly it guarantees nil initial conditions that are essential for the inverse problem to succeed.

The choice of parameters  $f_c$ ,  $t_0$  and  $t_1$  depends on the situation to be analyzed and thus they will have to be adjusted. For example,  $f_c$  must necessarily be lower than the minimum frequency of interest in the real motion of the system, but it must be high enough to efficiently remove all the likely divergence of the inverse problem. This will be effective only if the successive filters are also applied often enough, thus with a low value of the second parameter  $t_0$ . However, the latter must be high enough in order to have sufficiently new computed data to processed afterwards, namely several periods in the case of harmonic motion. Finally, the last parameter  $t_1$  will both control the length of the half-sine window function and the given amount of data retained at each new iteration of the filtering application. It is legitimate to define  $t_1$  as close as possible to  $t_0$  to ensure a smooth return to nil value, but this automatically increases the computational cost since more signal has to be recomputed. The influence of these three parameters is investigated further in Section 4.1.

To ensure more efficient solving, it is recommended to use this data processing on every angular displacement and its

respective angular velocity and acceleration during the time integration loop. In some cases, some discontinuities may appear in the solutions, where the original signals are substituted by their filtered ones at the transition  $t = t^* - t_0$ . Generally, this effect is more noticeable on the angular displacements whereas it may be drowned in the noise of the angular accelerations. To overcome this issue, a good way is to recompute the angular velocities and displacements by two additional successive integrations from the angular accelerations, for instance with a classical trapezoidal scheme, once the time loop finished and the whole signals obtained. Moreover, other high pass filters may be applied to the whole signals between these two time integrations, to ensure that no divergence can emerge back.

Finally, after all the angular variables have been computed and processed, the translational accelerations can be obtained through a new time loop with Eq. (19). In the same way as for the rotations, once the new loop is finished, the translational velocities and displacements may be computed from the translational accelerations with two successive trapezoidal time integrations combined with a high-pass filter on the whole duration of the signal.

As a complementary remark, it may also be relevant to filter the accelerograms used as inputs, prior to the inverse problem algorithm. On the one hand this helps to limit the study to a specific frequency range and, on the other hand, to anticipate any 0-Hz static components responsible for divergence issues. Nevertheless, special care must be taken when large rotations occur, in which case centripetal acceleration may exhibit non-negligible static components that must be accounted for. More details on this topic are given in Section 3.4.

For the sake of completeness, the different steps described in Sections 2.3 and 2.4 are summarized in the flowcharts of Fig. 5 and Fig. 6 corresponding to the rotation and translation problems, respectively.

### 3. EXPERIMENTAL VALIDATION

#### 3.1. Presentation of the experimental setup

An experimental investigation is carried out to validate the technique proposed. The device used is the 6-DOF hydraulic long stroke shaker from Team Corporation<sup>®</sup> presented in Fig. 7a, which is a cube with an edge of 0.8128 m able to provide accelerations up to 10 g within a frequency range of [0-250] Hz. Its motion is generated by the simultaneous displacement of three orthogonal pairs of hydraulic cylinders that can produce three translations and three rotations of the very stiff steel yellow fairing (which is considered perfectly rigid within the operational frequency band). To this fairing is attached the moving frame of reference  $R$ , represented in red in Fig. 7b. The position of this frame will depend on the test to be performed. That is to say, it varies according to where the instantaneous axis of rotation (passing through  $O$  in the case of rotational motion only) is to be located. Thus, to define the position of  $O$  a point  $C$  fixed to the shaker is used, irrespective of the test, located at the center of the upper face of the cube. The orientation of  $R$  will however always remain the same, with its axes directed toward the normal of each face of the shaker.

The shaker is driven by accelerometric data that are part of a closed loop algorithm. The latter compares the reference and measured accelerations after each iteration and corrects the motion accordingly afterwards. To obtain a specific motion defined in terms of six targeted displacements, a first direct problem (see Fig. 3) is applied to compute the targeted accelerometric data sent to the closed loop algorithm. The experimental accelerations corresponding to the real motion are then measured and used in this paper to solve the inverse problem and thus determine the real motion of the system. Nevertheless, the reliability of this inverse problem must first be certified in order to ensure that the differences between the targeted and calculated displacements do not originate from errors related to the inverse problem but rather from real physical phenomena. Since it is experimentally more convenient to use on-board sensors, this validation is performed with accelerometers and gyroscopes instead of sensors measuring displacements. In this context, since the solution of the inverse problem gives the six displacements of the system, the idea is to use them as the inputs of a second direct problem as shown in Fig. 3, to obtain the “numerical” linear accelerations and angular velocities to be compared with the experimental ones provided by other sensors not already used in the inverse problem. In order not to create any confusion between the three different sets of data involved, specific adjectives are used throughout the further sections: targeted for the motion and accelerations that are to be reproduced by the shaker, calculated for the data related to the solution of the inverse problem, and real for the data related to physical and measured phenomena.

Thus, the shaker is instrumented with three sets of sensors. The first one is composed of four tri-axial PCB ICP<sup>®</sup> 356A15 accelerometers located at the four vertices of the upper face (rows 1 to 4 of Table 1), with sensitivity of 100 mV/g. They are used exclusively for the inverse problem. Although there are more data than required for the latter to work, only six accelerograms among the twelve available of Table 2 will be used in every case as this is a requirement of the present paper. The tri-axial information will be useful to investigate the influence of the sensor’s direction and position, which is described in Section 4.2. The second set of sensors is composed of six mono-axial PCB ICP<sup>®</sup> 333B40 accelerometers located by pairs on three orthogonal faces (rows 5 to 10 of Table 1), with a higher sensitivity of 500 mV/g.

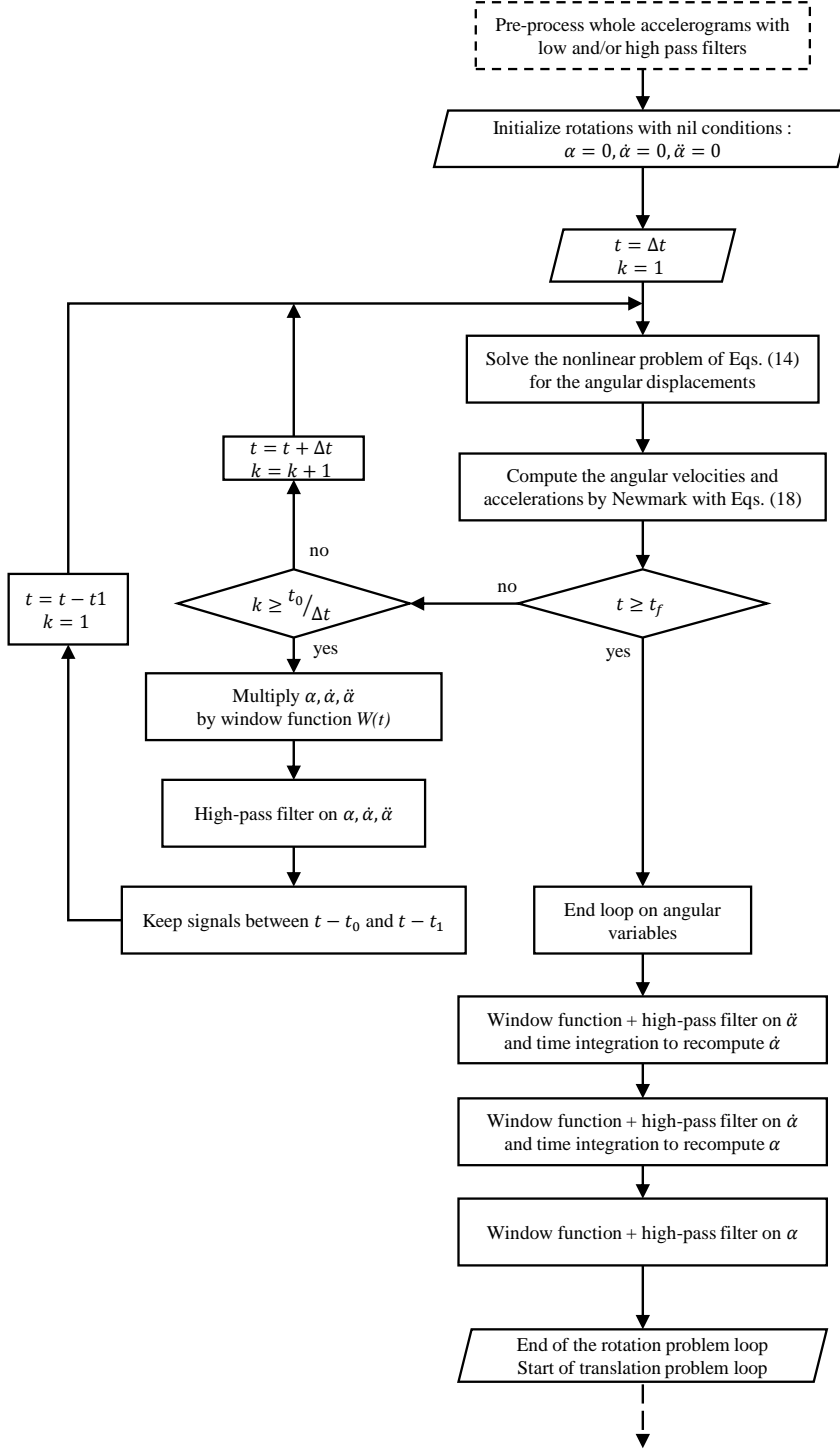


Figure 5: Block diagram of the numerical and data processing to obtain the 6 DOFs - Rotation problem

They are used exclusively for both driving the system (first direct problem) and the validation (second direct problem). The collection of data related to these tri and mono-axial accelerometers is done by a DataPhysics acquisition system, permitting synchronous time acquisitions with sampling up to 42 kHz. A third set of sensor is used, composed of four Delsys<sup>®</sup> Trigno IM providing both tri-axial accelerations and tri-axial gyroscopes (rows 11 to 14 of Table 1). They are

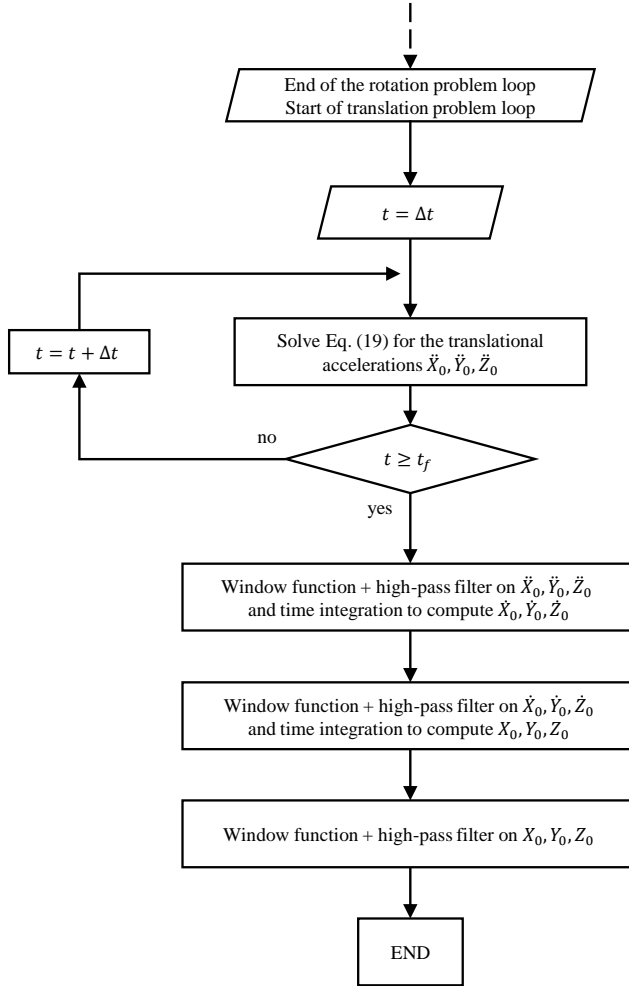


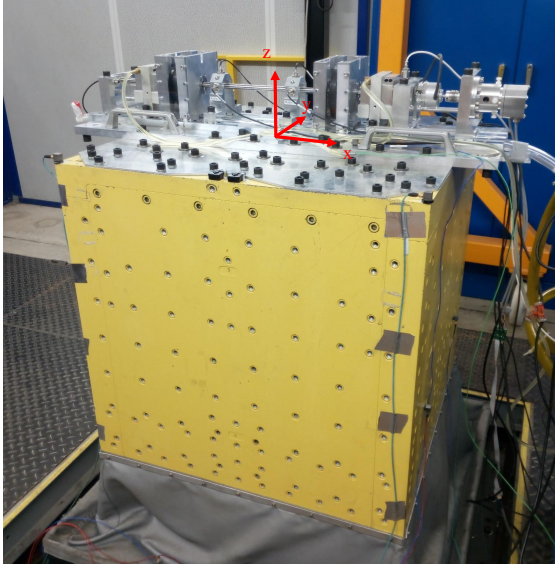
Figure 6: Block diagram of the numerical and data processing to obtain the 6 DOFs - Translation problem

used exclusively for the validation step. Since the latter were originally designed for sports monitoring and biomedical applications, the connections are ensured through Wi-Fi and consequently the sampling frequency is relatively low, that is to say 147 Hz. The accelerations and angular velocities provided with these sensors are respectively up to 16 g and 2500 °/s.

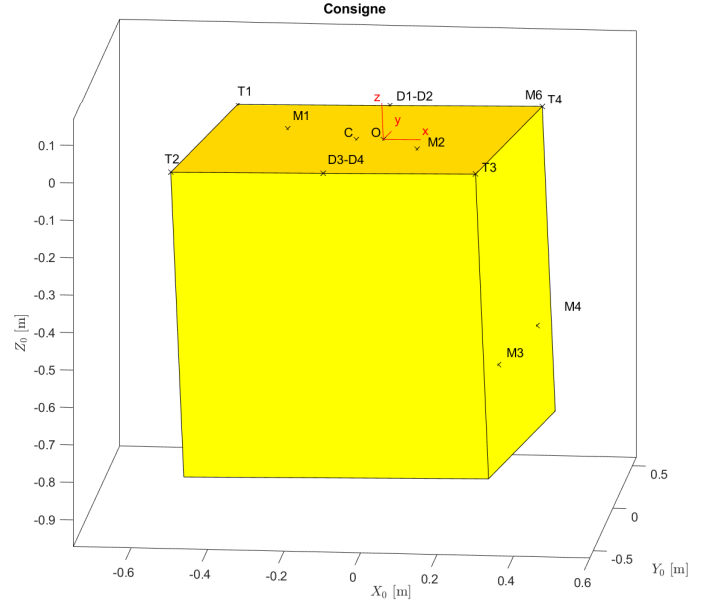
For all the further cases, the Galilean frame of reference  $R_0$  initially has the same orientation as  $R$ , namely the rotations do not have static values when the system is at rest. Regarding all the experimental validations, unless explicitly mentioned, the sampling frequency is  $f_e = 1024$  Hz and all the accelerograms used as inputs of the inverse problem are pre-filtered with high-pass and low-pass cut-off frequencies of 450 Hz and 1.5 Hz, respectively. Besides, the gravitational participation has been removed since the piezo-electric accelerometers used cannot deal with low frequencies and the variations of angle involved are too low. All the computations were performed on a Windows 10 environment using a i7-6820HQ CPU with 2.70GHz.

### 3.2. Harmonic motion with two combined rotations

For the first validation case, a two-axial sinusoidal rotation of the system is defined around the axes  $\vec{Z}_0$  and  $\vec{Y}_2$  defined respectively by the angular displacements  $\alpha_1(t) = A_1 \cos(2\pi f_1 t + \varphi_1)$  and  $\alpha_3(t) = A_3 \cos(2\pi f_3 t + \varphi_3)$  with  $A_1 = A_3 = 0.1$  °,  $f_1 = 16.875$  Hz,  $f_3 = 11.25$  Hz,  $\varphi_1 = 180$  °,  $\varphi_3 = 137$  ° and  $t$  the time parameter varying in  $[0; 16]$  s. With these two frequencies involved and even with the combination of their harmonics of type  $|pf_1 \pm qf_2|$  where  $(p, q)$  are any set of natural integers, this case is periodic with a frequency of 5.625 Hz. The origin  $O$  of  $R$ , through which the instantaneous



(a) Presentation of the 6-DOF shaker with an on-board structure



(b) Sketch of the 6-DOF shaker

Figure 7: Experimental setup

Sensor ID	Sensing direction	x [m]	y [m]	z [m]
T1	$x, y, z$	-0.4064	0.4064	0
T2	$x, y, z$	-0.4064	-0.4064	0
T3	$x, y, z$	0.4064	-0.4064	0
T4	$x, y, z$	0.4064	0.4064	0
M1	$z$	-0.2094	0.1194	0
M2	$z$	0.1864	-0.1164	0
M3	$x$	0.4064	-0.2350	-0.5461
M4	$x$	0.4064	0.2350	-0.5461
M5	$y$	0	0.4064	-0.1400
M6	$y$	0.4064	0.4064	0
D1	$x, y, z$	0	0.4064	0
D2	$x, y, z$	0	0.4064	0
D3	$x, y, z$	0	-0.4064	0
D4	$x, y, z$	0	-0.4064	0

Table 1: List of sensors used and their coordinates in  $R$  with respect to the center  $C$  of the upper face of the shaker

axis of rotation must pass, is shifted from  $C$  in  $\vec{x}$  by 0.0714 m and 0 m in the other axes, as shown in Fig. 7b. The origin  $O_0$  of  $R_0$  is defined so as to be coincident with  $O$ , therefore the translations have nil static values. This motion is sent to the closed loop driving algorithm and the experimental accelerations are collected to solve the inverse problem. The three parameters of the latter are defined as  $f_c = 1.5$  Hz,  $t_0 = 0.3$  s and  $t_1 = 0.2$  s. It can be noted that  $f_c$  is chosen far enough from the minimum frequency involved here and that  $t_1 < t_0$ . The accelerograms used for the rotational part of the inverse problem according to Eq. (15) and Table 2 are  $i_1 = 1$ ,  $j_1 = 4$ ,  $i_2 = 3$ ,  $j_2 = 6$ ,  $i_3 = 3$  and  $j_3 = 12$ . It must be emphasized that only 5 accelerograms are used since  $i_2 = i_3$ . The choice of these five accelerograms has not been done arbitrarily but is the result of a previous research devoted to reducing the average condition number of the matrix  $[T]$  of Eq. (16), which is in this case equal to 1.00013. More details about this matrix are given in Section 4.2. Regarding the translation problem which requires the tri-axial acceleration at the same location, and given the accelerograms already used for the rotations, both accelerograms 2 and 5 of Table 2 could be used to solve Eq. (19). Here, the former was chosen arbitrarily.

Accelerogram number	Sensor ID	Direction
1	T1	$x$
2	T1	$y$
3	T1	$z$
4	T2	$x$
5	T2	$y$
6	T2	$z$
7	T3	$x$
8	T3	$y$
9	T3	$z$
10	T4	$x$
11	T4	$y$
12	T4	$z$

Table 2: Numbering of the accelerogram to be used in the inverse problem

Since it is a rotational motion, the first obvious validation is done the gyroscopes from Delsys<sup>®</sup>. In addition, tangential acceleration is detected by the accelerometers, then the second validation is made with the mono-axial accelerometers from PCB<sup>®</sup> which provide better quality than those from Delsys<sup>®</sup>. The results are compared in the time domain with time history responses and in the frequency domain by applying Fast Fourier Transform to the periodic part of the test only (between the beginning and the end of the shaker’s motion). For the sake of clarity, only a small part of these curves is shown in the time domain, but at the end of the test where the error accumulation is expected to be greater. The Fourier transforms are normalized by the length of the signal and plotted in dB with  $1^\circ/s$  and 1 g as the dB references. In this example, comparisons are made with the main angular velocities and linear accelerations involved, namely  $\omega_y^0, \omega_z^0$  (components in  $\vec{y}$  and  $\vec{z}$  of the frame  $R$  of the angular velocity vector of Eqs. (5)) and  $\gamma_{\vec{x}}$  (acceleration in  $\vec{x}$  of the frame  $R$ ), respectively with sensors D1 and M3 of Table 1 in Fig. 8 and Fig. 9. In view of these first results, it can be emphasized that the REDEAT method is highly reliable, in both the time and frequency domains, and both translation and rotation. However, slight discrepancies may be noted, especially in the angular velocities. This can be explained with the lower quality of the gyroscopes employed with respect to the tri-axial accelerometers used in the inverse problem. In particular, spurious frequency peaks appear due to aliasing that are not present in the inverse problem results due to the preliminary application of low-pass filters and the higher sampling frequency. Furthermore, noise is much more significant with the gyroscopes as can be seen in the spectral responses of Fig. 8. Regarding the linear accelerations, outstanding agreement is observed between the two results and the noises are relatively similar. Only a small difference can be noted with the presence of one spurious frequency peak predicted by the inverse problem around 28 Hz. Nevertheless their amplitudes remain acceptable. The computational cost required to performed the whole inverse problem described in Section 2.3 and 2.4 was only 105 s for a measurement length of 17677 (17.26 s for the sampling of 1024 Hz used).

Once the proposed technique has been validated, the calculated results of the inverse problem can be considered representative of the real physical motion of the shaker. Thus, it is of great interest to assess the error between the targeted motion and the real-calculated experimental motion. Therefore, the 6 DOFs ( $X_0, Y_0, Z_0, \alpha_1, \alpha_2, \alpha_3$ ) of the shaker, are shown in Fig. 10a and Fig. 10b. The targeted translations are not presented since they are all nil, as defined by the conditions of the test. Only the beginning and a small part of the signals are presented here in order to better distinguish the different curves and show the transient part when motion starts. These results demonstrate that the targeted motion is globally faithfully reproduced, especially for the rotation of angle  $\alpha_1$ . The rotation of angle  $\alpha_3$  is, in contrast, slightly lower than expected, yielding  $0.09^\circ$  instead of the  $0.1^\circ$  imposed. Regarding the other DOFs that should be nil, an extra rotation of angle  $\alpha_2$  is present, which represents up to 20 % of the other rotation references. Moreover, three translations also act with a maximum value of 0.102 mm in  $\vec{X}$ . Therefore, the actual instantaneous axis of rotation no longer coincides with the targeted one, especially for the instants of time when only translational velocities remain ( $\dot{\alpha}_1 = \dot{\alpha}_2 = \dot{\alpha}_3 = 0$ ). However, even in this case, this level of additional translation may appear insignificant when considering in terms of accelerations, which are responsible for inducing additional forces on an on-board structure installed on the shaker. If pure rotation is wanted, which is the case here, what matters is to ensure that the participation of these translations in acceleration is sufficiently lower than the linear accelerations normally produced by the rotation on key locations of the on-board structure tested. For instance, the ratio in RMS (Root Mean Square) of  $\vec{X}_0$  with respect to the previous

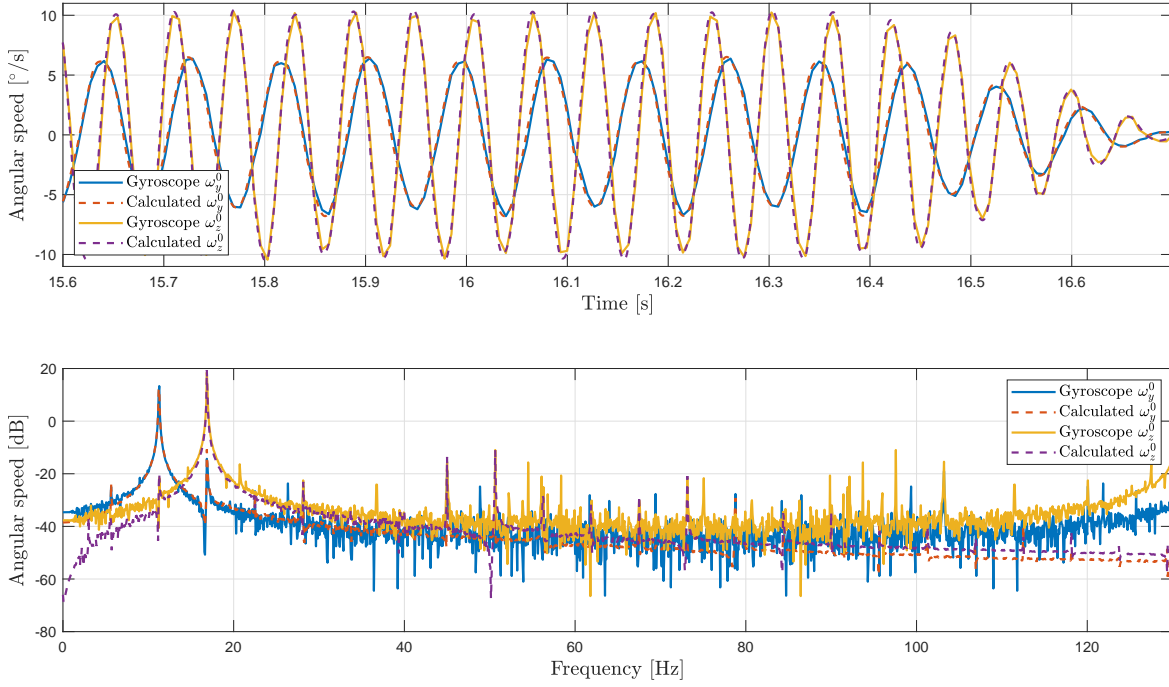


Figure 8: Comparison between calculated and real (with gyroscope D1 of Table 1) angular speeds for harmonic motion in the time and frequency domains

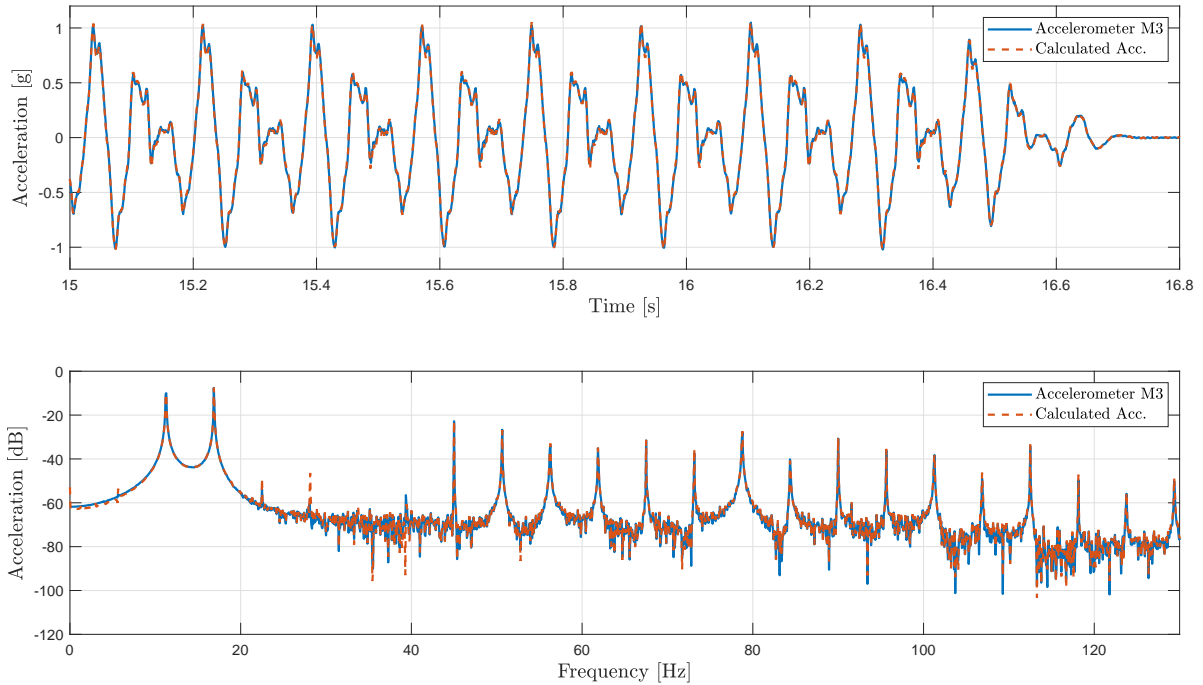


Figure 9: Comparison between calculated and real (with accelerometer M3 of Table 1) linear accelerations in  $\vec{x}$  of  $R$  for harmonic motion in the time and frequency domains

acceleration shown in Fig. 9 is only 13.42 %. This can be reduced for other directions and locations. Of course, the cross-sensitivity of the sensors to the transverse directions may also introduce bias in this evaluation.

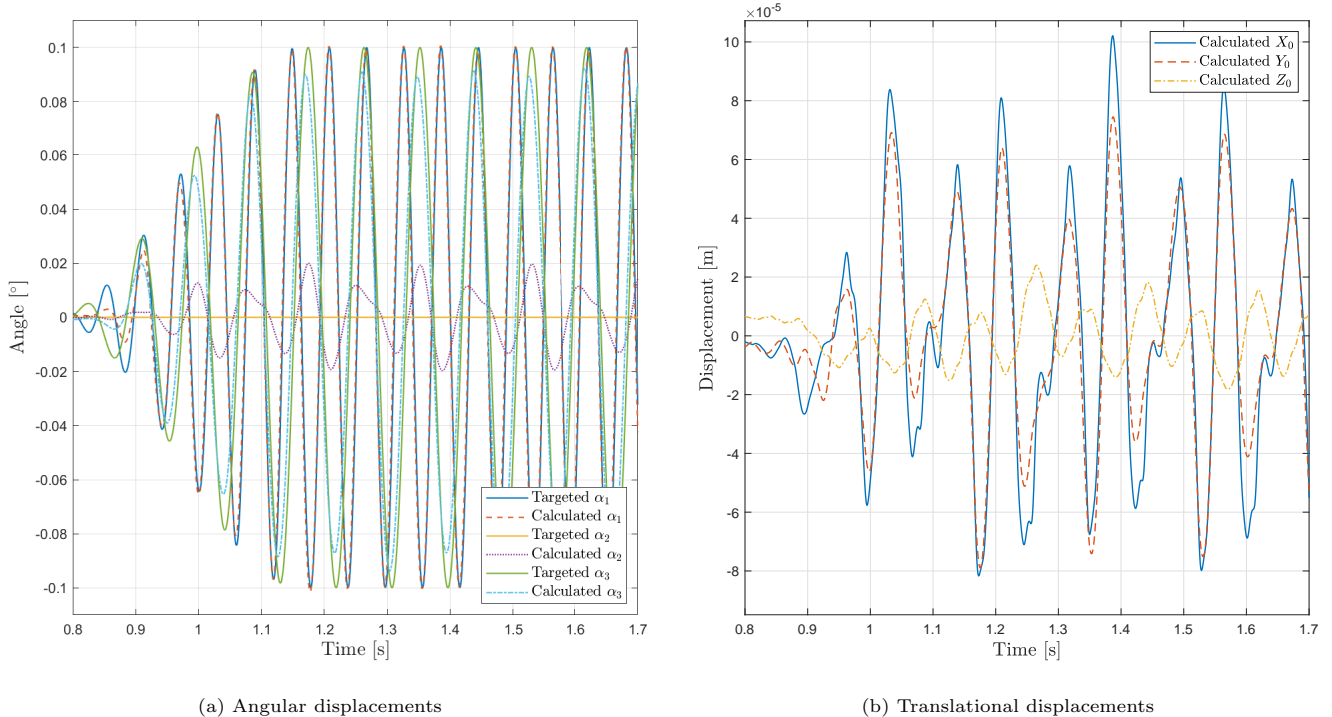


Figure 10: Comparison between targeted and calculated motions

### 3.3. 6-DOF random motion

In order to highlight the accuracy of the REDEAT method with any possible case, a second test consisting in complete multi-axial motion with 6-DOF random motion is addressed. To this end, since no specific motion is desired, no first direct problem is run to obtain targeted accelerations to be sent to the driving system process. Instead, random time signals defined by the same white noise are sent directly to the shaker, generating the random displacement of the six hydraulic actuators. The spectral content of this white noise is defined through a Power Spectrum Density (PSD), which is nonzero in [4-40] Hz and nil everywhere else. The duration of the random signal is approximately 27s. In contrast with the previous sinusoidal combined rotations test, the location of  $O$  is of no importance in this random test, hence it is defined so as to be coincident with  $C$ . Likewise for  $O_0$  for the system at rest. The three parameters of the inverse problem are kept as with the previous case, at  $f_c = 1.5$  Hz,  $t_0 = 0.3$ s and  $t_1 = 0.2$  s. Once again,  $f_c$  has been chosen far enough from the minimum frequency of 4 Hz involved here. The choice of the accelerograms used for the rotation and translation problems remain the same as before. Thanks to the 6-DOF motion, a complete validation can be established by comparing all the angular speeds ( $\omega_x^0, \omega_y^0, \omega_z^0$ ) and the linear accelerations ( $\gamma_{\bar{x}}, \gamma_{\bar{y}}, \gamma_{\bar{z}}$ ) detected in  $R$  by specific sensors fixed to the shaker. This is done respectively with the three gyroscopes of sensor D1 and accelerometers M3, M5 and M1 of Table 1. Acquisition is done before the motion starts and after it stops, so that the actual measurement duration is 30 s. The calculated results are compared with the measured data in the time domain with time history responses and in the frequency domain by computing the PSD of the response during the random part of the test only, i.e. between 1 s and 28 s. These PSDs are plotted in dB/Hz with  $1^\circ/s$  and 1 g as the dB references.

Even for a complete multi-axial motion with a random profile, excellent prediction capabilities of the REDEAT method can be noted through the comparisons shown in Fig. 11 and Fig. 12. Once again, greater differences are seen with the gyroscopes, owing to their lower sampling, aliasing and higher noise. Regarding the accelerometers, the signals are extremely similar, even for low acceleration values and at low frequency despite the technology used. The computational cost required for this case was only 167 s for a measurement length of 30721, which can be considered as satisfactory.

### 3.4. Simulated case with larger rotations

The main drawback of the 6-DOF shaker used previously is that it cannot produce large angular displacements. This restricts the solving of the inverse problem to a linear system of equations. An alternative proposed to demonstrate its accuracy even for nonlinear problems is to impose larger rotations on a simulated version of this 6-DOF shaker. To

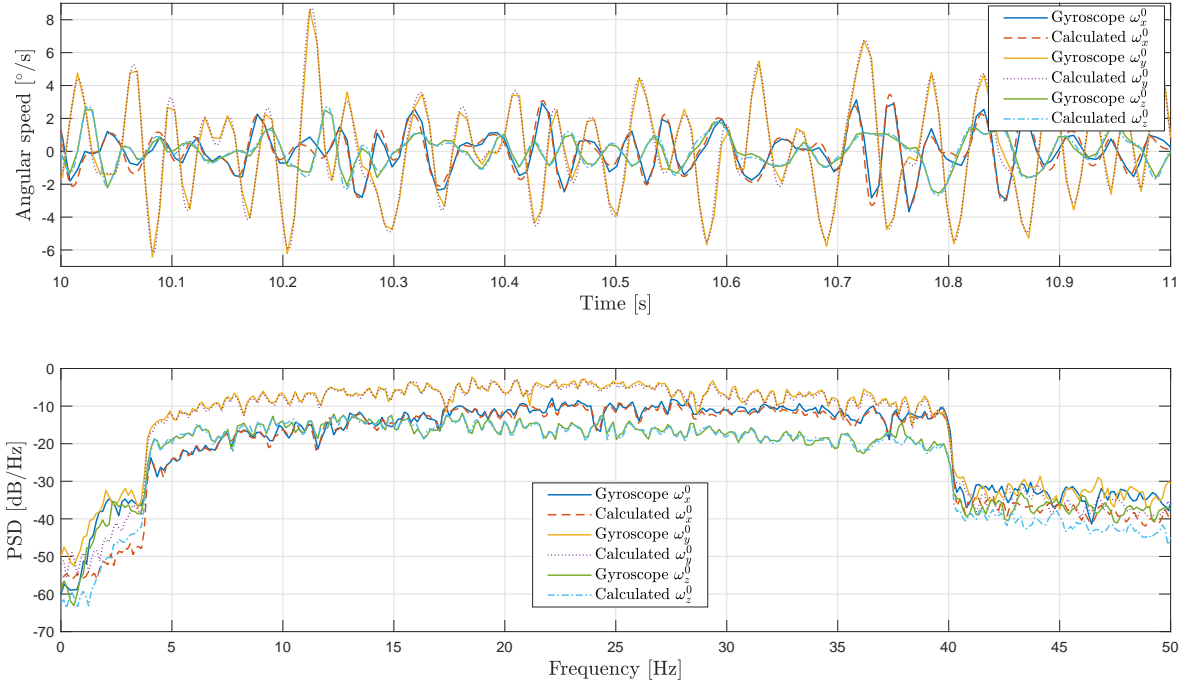


Figure 11: Comparison between calculated and real (with gyroscope D1 of Table 1) angular speeds for random motion in time and frequency domains

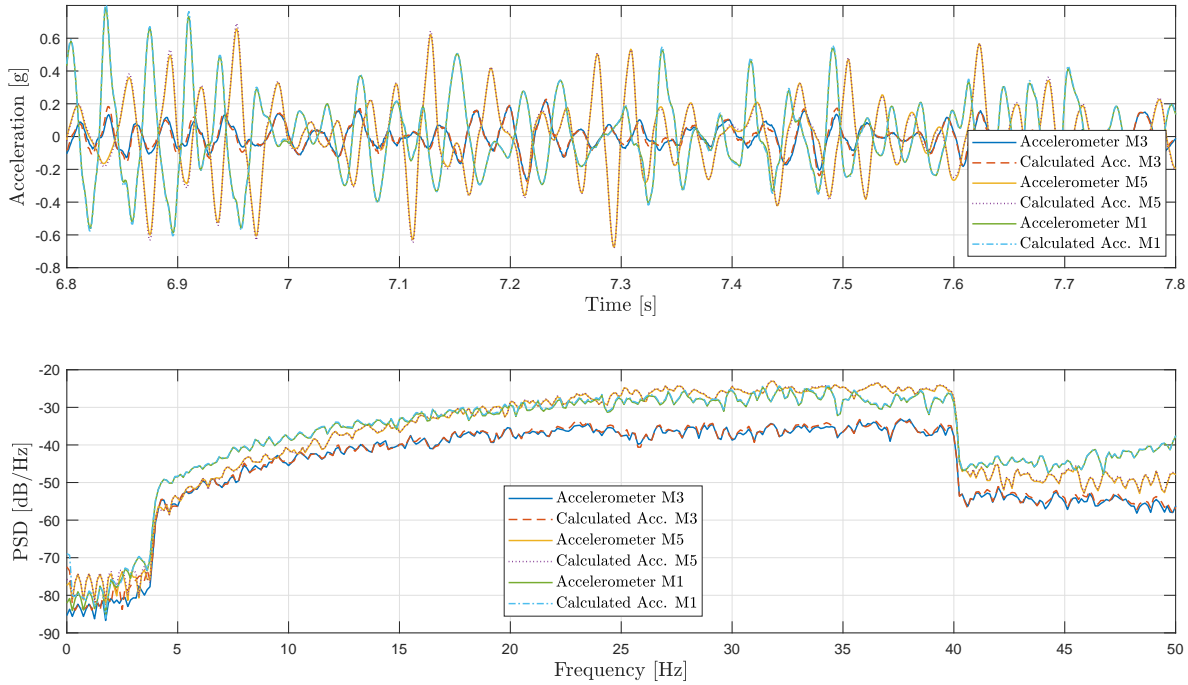


Figure 12: Comparison between calculated and real (with accelerometers M3, M5 and M1 of Table 1) linear accelerations in  $\vec{x}$ ,  $\vec{y}$  and  $\vec{z}$  of  $R$  for random motion in time and frequency domains

this end, a specific targeted motion is sent to the direct problem illustrated in Fig. 3 and the accelerations detected by theoretical accelerometers, located at the same locations as those described previously and listed in Table 1, are computed.

In order to be more representative of real experimental conditions, a Gaussian white noise is added to these accelerations. Then, the resulting accelerograms are sent to the inverse problem to obtain the corresponding calculated 6 DOFs. The main advantage of this approach is that the real solution in displacement is known since it is that which is used as the input for the direct problem, namely the targeted motion. Hence, the validation of the inverse problem can be performed directly in terms of displacements instead of angular velocities or accelerations as in the experimental cases of Sections 3.2 and 3.3.

The case study comprises a two-axial harmonic rotation, defined around axes  $\vec{Z}_0$  and  $\vec{X}_1$  with angles  $\alpha_1 = A_1 \cos(2\pi t f_1 + \varphi_1)$  and  $\alpha_2 = A_2 \cos(2\pi t f_2 + \varphi_2)$ , such as  $A_1 = 50^\circ$ ,  $A_2 = 40^\circ$ ,  $f_1 = f_2 = 1$  Hz,  $\varphi_1 = 57^\circ$  and  $\varphi_2 = 91^\circ$ . These low frequencies were chosen intentionally, so as to limit the angular and linear accelerations that could be quite significant for this value of amplitude, and thus remain in an experimentally viable framework. The origin  $O$  of  $R$  is shifted from  $C$  by 0.114 m, 0.0285 m and -0.33 m along the axes  $\vec{x}$ ,  $\vec{y}$  and  $\vec{z}$ , respectively. Moreover, nil static translational values are considered so that  $O_0$  and  $O$  are theoretically coincident. The time varies in  $[0-19.6]$  s with a time step of  $\Delta t = 1/1024$  s. The noise added to the accelerograms is defined by a Gaussian random process with zero-mean and a standard value deviation of 0.0045 g, typical of that exhibited by the tri-axial accelerometers of Table 1. In addition, the sinusoidal motion is modified to simulate a smooth start-up and stop of the system and thus avoid infinite angular accelerations. This is done by multiplying the angles  $\alpha_1$  and  $\alpha_2$  with a window function similar to that in Fig. 4b, built such that it is unitary for  $t \in [4; 15]$  s and nil for  $t \leq 3$  s and  $t \geq 16$  s. Meanwhile, the sinusoids are delayed by 3 s, so that the cosine has phases  $\varphi_1$  and  $\varphi_2$  when the motion starts at  $t = 3$  s. The value of the three parameters of the inverse problem are chosen as  $f_c = 0.3$  Hz,  $t_0 = 3$  s and  $t_1 = 2.8$  s. These parameters were adjusted according to the aspect mentioned in Section 2.4. In particular,  $t_0$  was chosen high enough to account for several periods of the excitation and  $t_1$  must be relatively close to  $t_0$  in order to avoid any jump between two successive time iterations typical of nonlinear problems and which produces extreme divergences in numerical solving. The accelerograms used for the inverse problem are the same as in the previous experimental cases. The computational time consumed was about 167 s for this case, with a measurement length of 20068.

The results in terms of the angular displacements  $(\alpha_1, \alpha_2, \alpha_3)$  and the translational displacements  $(X_0, Y_0, Z_0)$  are shown in Fig. 13 and Fig. 14, respectively. Once again, since the targeted  $(X_0, Y_0, Z_0)$  are nil, the corresponding curves are not shown. It is noteworthy that the rotations of angle  $\alpha_1$  and  $\alpha_2$  are well predicted, in both amplitude and frequency, especially in the periodic part of the test. However, a slight discrepancy may be pointed out when the motion starts and ends. The other rotation of angle  $\alpha_3$  does not exceed the value of  $2^\circ$  which is relatively reasonable with respect to the other ones. Likewise, the translational displacements are quite small, remaining below 2.1 cm, which is considerably lower than the overall displacements undergone by any rotating part of the system for such large rotations. All these errors can first be explained by the noise added to the accelerograms. But the main source of error actually comes from the proximity of the cut-off frequency  $f_c$  of the high-pass filters at the frequency of 1 Hz involved in the rotations. For such cases, a delicate compromise has to be found between a high value of  $f_c$  that permits efficiently removing as many low frequencies (responsible for divergence due numerical integration) as possible or a low value that permits filtering far away from the frequencies of the excitations involved. In the present case,  $f_c = 0.3$  Hz appeared the best choice. In cases for which the frequencies of excitations are even lower, it might be difficult to find a satisfactory value for  $f_c$  and thus converge toward a reliable solution. This might represent one drawback of the REDEAT method.

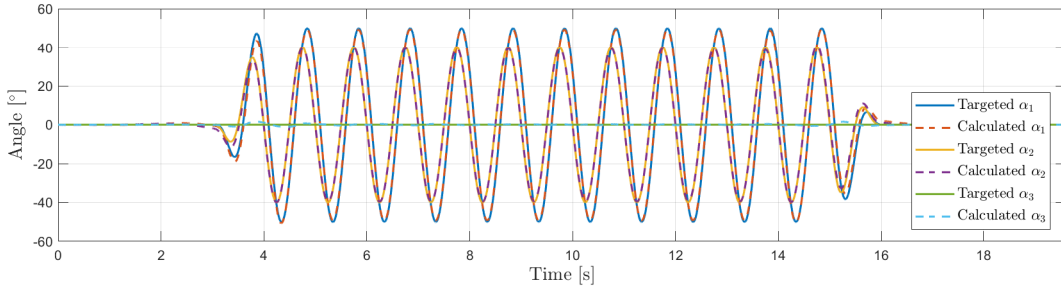


Figure 13: Comparison between calculated and targeted angular displacements for large rotations

If large rotations are required experimentally, special care must be taken. Indeed, in this case, centripetal accelerations may exhibit 0-Hz components of the same order as the main frequency of the tangential accelerations. For example, for a mono-axial rotation of  $\alpha_1 = A_1 \cos(2\pi t f_1)$  with  $A_1 = 50^\circ$  and an arbitrary radius  $R$ , the centripetal acceleration

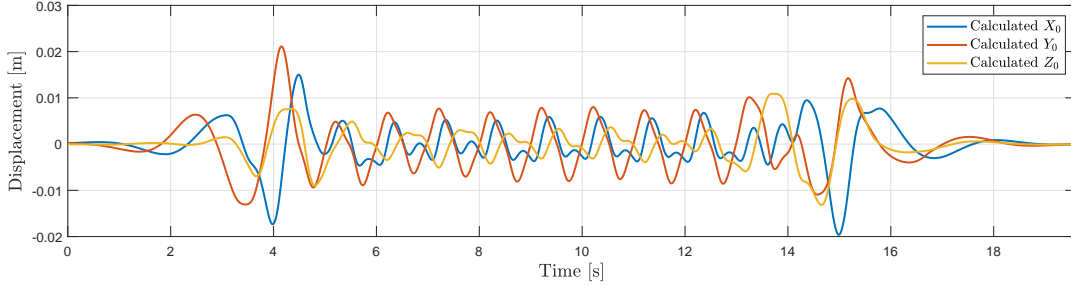


Figure 14: Comparison between calculated and targeted (nil) translational displacements for large rotations

$-R(\dot{\alpha}_1)^2$  has a 0-Hz static component that represents about 0.44% of the  $f_1$ -Hz component of the tangential acceleration  $R\ddot{\alpha}_1$ . While for small rotations it is relevant to orient the accelerometers in the tangential direction where accelerations are dominant, in larger rotations this might produce bias error due to the inherent cross-sensitivity of the sensors. In addition, it is important to use sensors that can yield 0-Hz components in order to preserve the full accelerometric data. Of course, these constant accelerations must not be removed prior to the inverse problem with a high-pass filter.

#### 4. INFLUENCE OF IMPORTANT PARAMETERS

##### 4.1. $f_c, t_0, t_1$ and window function

As described in Section 2.4, the inverse problem proposed in the present paper includes three parameters. Each one has its own role and thus needs to be adjusted. To illustrate this, the experimental random test of Section 3.3 is reused, with the same parameters, unless otherwise specified. First, the influence of the cut-off frequency  $f_c$  in the inverse problem solution is addressed. To do this, several values are defined between 0 Hz and the minimum frequency of 4 Hz of the DSP, such as  $f_c = [0.1; 0.5; 1; 2; 3]$  Hz, while  $t_0 = 0.3$  s and  $t_1 = 0.2$  s. Owing to the better quality of the accelerometers, only the accelerations are used as a basis for comparison. Moreover, only sensor M3 which shows the highest errors is displayed in order to lighten the figure. Since differences are more visible in the spectrum, only the DSP of the responses is presented here in the low frequency range of [0-11] Hz. The corresponding curves are presented in Fig. 15. It can be seen that most of the effects are noted in low frequency. As expected, for the lowest value of  $f_c$ , the calculated solution provides a significant biased estimation below 1 Hz, since the divergence has not been efficiently removed. The low frequency portion can be considered satisfactory from  $f_c$  of 1 Hz. Above 4 Hz, it is demonstrated that a cut-off frequency higher than 3 Hz already starts underestimating the frequency range of interest of the DSP. Therefore, for this case a good compromise can be found between  $f_c = 1$  Hz and  $f_c = 2$  Hz.

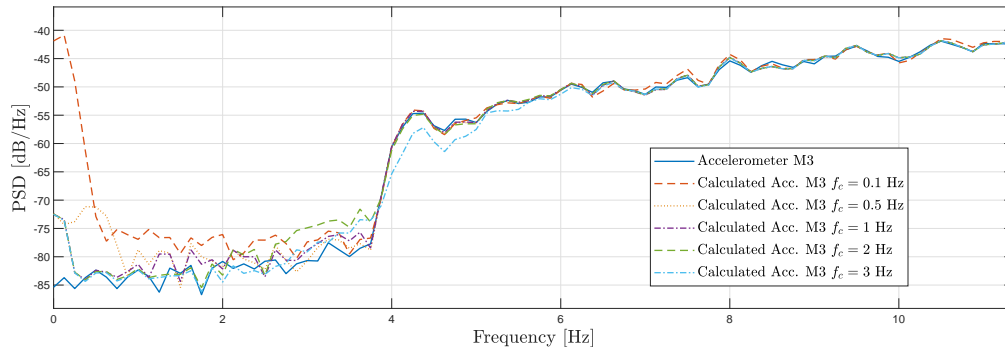


Figure 15: Influence of the cut-off frequency of the successive high-pass filters

In order to reduce the time costs, the successive high-pass filters can be employed fewer times by increasing the value of  $t_0$ , to the detriment of the accuracy of the solution. Once again, only the accelerations are used for the comparison, however for the three sensors M3, M5 and M1 of Table 1. Nevertheless, since the discrepancy is sometimes hardly visible in both the time and frequency domains, the influence of  $t_0$  is assessed through the following error indicator  $\varepsilon = \text{RMS}(ref - sol) / \text{RMS}(ref)$ , where RMS is the Root Mean Square value of the time series,  $ref$  is the accelerometer

signal and  $sol$  is the solution of the inverse problem. These RMS values are computed on the random part of the motion, between  $t = 1$  s and  $t = 28$  s. In this way, several values of  $t_0$  are tested, such as  $t_0 = [0.3; 1; 2; 3; 4; 5; 10]$  s, while  $f_c = 1.5$  Hz and  $t_1 = 0.2$  s. The results are presented in Table 3. The first comment to be emphasized is that the error indicator  $\varepsilon$  may seem relatively high, even for low values of  $t_0$  around 0.3 s, where the tendency appears to converge. This can be explained by several reasons. Firstly, the reference used here has its own bias, due to measurement noise, cross-sensitivity and calibration bias, making it an imperfect reference basis. Secondly, the six accelerograms used in the inverse problem are also obtained from sensors each one having its own bias. Thus, even for the best optimized values of  $f_c$ ,  $t_0$  and  $t_1$  and good agreements such as that shown in Fig. 12, it is normal to remain with an  $\varepsilon$  of this order. That being said, on looking at Table 3 it can be highlighted that, as expected, the accuracy of the REDEAT method deteriorates as the successive filters are applied less frequently. Nevertheless, keeping the same value of  $t_1 = 0.2$  s efficiently reduces the computational cost. This cost presents some large gaps, for instance from  $t_0 = 0.3$  s to  $t_0 = 1$  s or from  $t_0 = 2$  s to  $t_0 = 3$  s. This is due to the integer number of time returns in the algorithm of Fig. 5 (namely when  $t$  is substituted for  $t - t_1$ ), which is a piecewise constant function of  $t_0$ . This cost also seems to converge toward an asymptotic value, around 74 s. This is the time cost normally required to solve the rotation problem of Fig. 5 directly, without moving backward in time. In view of these results, a good compromise between accuracy and time cost could be obtained for  $t_0 = 1$  s. Finally, it should be emphasized that the error indicator  $\varepsilon$  is higher in  $\vec{x}$  (M3) than the other one, because it is the direction with less acceleration, as seen in Fig. 12, thus subject to more noise error.

$t_0$ [s]	0.3	1	2	3	4	10
$\varepsilon$ M3 [%]	21.41	21.44	24.69	33.77	121.98	216.96
$\varepsilon$ M5 [%]	13.22	13.25	15.95	21.88	79.44	127.95
$\varepsilon$ M1 [%]	10.80	10.81	11.13	11.98	39.96	65.85
<b>Time cost [s]</b>	167	84	83	76	75	74

Table 3: Influence of the second parameter  $t_0$  on  $\varepsilon = \text{RMS}(ref - sol) / \text{RMS}(ref)$

Finally, the last parameter to be investigated is  $t_1$ , which controls both the length of the half-sine window function and the interval of time to be retained at each successive filter application. As for  $f_c$ , the influence of this parameter is mostly seen at low frequency and only the acceleration along  $\vec{x}$  with M3 is analyzed. Thus, four values of  $t_1$  are tested, such as  $t_1 = [0.01; 0.1; 0.2; 0.25]$  s, while  $f_c = 1.5$  Hz and  $t_0 = 3$  s. In addition, the inverse problem is also solved without the use of  $W(t)$ , to emphasize the effect of the window function. The results are presented in Fig. 16. The corresponding computational cost for  $t_1 = [0.01; 0.1; 0.2; 0.25]$  s are 76 s, 98 s, 167 s and 346 s, respectively. As expected, not resorting to the window function provides bad predictions at low frequency. The conclusion is the same for the low value of  $t_1$ , below 0.1 s. In contrast, when  $t_1$  is closer to  $t_0$ , the results improve significantly and seem to converge toward the reference, except for the very low frequencies below 0.25 Hz. For higher frequencies, however, above 5 Hz, the results are quite similar and become closer as the frequency increases. It can be concluded that increasing the value of  $t_1$  improves the accuracy of the REDEAT method, to the detriment of the computational cost which are more than doubled from  $t_1 = 0.2$  s to  $t_1 = 0.25$  s.

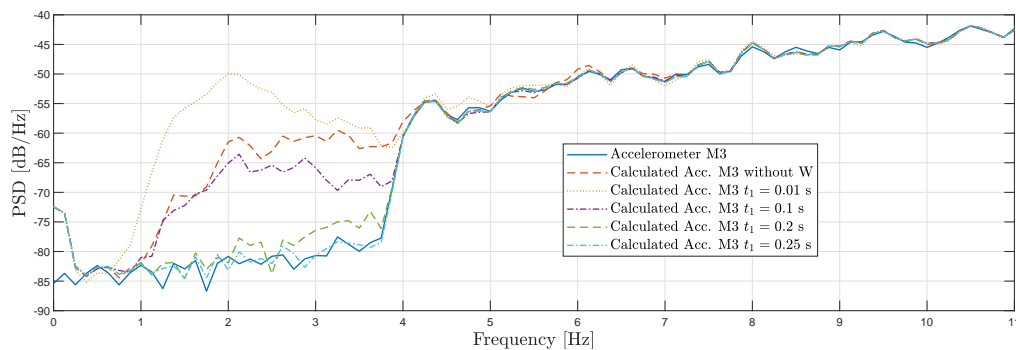


Figure 16: Influence of the third parameter  $t_1$

#### 4.2. Influence of accelerometers directions and positioning

As the 6-DOF shaker is equipped with four tri-axial accelerometers fixed in one plane, their twelve accelerograms numbered in Table 2, are available to solve the inverse problem. Nevertheless, as it is a prerequisite of the paper proposed, only six accelerograms are used, which leaves a lot of possibilities. Clearly, all the configurations are not all suitable, because, for instance, not all the accelerograms must be oriented all along the same direction. It is therefore expedient to seek which are the best configurations and thus assess the influence of the direction and position of the sensors on the results calculated by the inverse problem. Only the rotation problem described in Section 2.3 and illustrated in Fig. 5 is treated here since it is that most subject to divergence issues. Therefore, it is necessary to choose three subtractions of two accelerograms having the same orientation and belonging to different sensors. These three subtractions need not necessarily represent all three directions  $(\vec{x}, \vec{y}, \vec{z})$ , as shown by the configuration used in Sections 3.2 and 3.3 which uses only subtractions in  $\vec{x}$  and  $\vec{z}$ . Moreover, the same accelerograms can be used several times. Choosing subtractions of two accelerograms having the same direction from the twelve accelerograms, and eliminating the redundant subtractions results in a large number of lists of nine-linearly-independent subtractions. One of them is presented in Table 4. It should be mentioned that, as only three subtractions are required for determining the three rotations  $(\alpha_1, \alpha_2, \alpha_3)$ , 84 combinations of three subtractions are possible in each list of nine-linearly-independent subtractions.

Subtraction number	Accelerograms subtractions
1	T1x - T2x (1-4)
2	T1y - T2y (2-5)
3	T1z - T2z (3-6)
4	T1x - T3x (1-7)
5	T1y - T3y (2-8)
6	T1z - T3z (3-9)
7	T1x - T4x (1-10)
8	T1y - T4y (2-11)
9	T1z - T4z (3-12)

Table 4: An example of a list of nine-linearly-independent-subtractions, three subtractions must be extracted from them for the rotation problem (the numbers in parenthesis refer to Table 2)

As mentioned in Section 2.3, a major initial factor for the success of the algorithm is to ensure a low condition number of the tangent matrix  $[T]$  of Eq. (16). This number, which can be computed as the ratio of the maximum singular value of the matrix to the minimum one, represents how sensitive the errors in the results are to the errors in the inputs of the problem. Thus, its variation with respect to the choice of the accelerograms helps to make a preliminary choice from these 84 combinations of three subtractions. A good way to achieve this goal is to analyze the algorithm stability when the system is at rest, namely when there are no angular displacements, velocities or accelerations. In the latter case, the rows of the tangent matrix  $[T]$  simplifies as  $a_0 \begin{bmatrix} -(y_i - y_j) & 0 & (z_i - z_j) \end{bmatrix}$ ,  $a_0 \begin{bmatrix} (x_i - x_j) & -(z_i - z_j) & 0 \end{bmatrix}$  or  $a_0 \begin{bmatrix} 0 & (y_i - y_j) & -(x_i - x_j) \end{bmatrix}$  when the direction related to the corresponding subtractions is in  $\vec{x}$ ,  $\vec{y}$  or  $\vec{z}$ , respectively. The indexes  $(i, j)$  are two integer subscripts from 1 to 12, denoting the two accelerograms corresponding to one subtraction in Table 4, and  $(x_i, y_i, z_i)$  and  $(x_j, y_j, z_j)$  are the coordinates in  $R$  of the two corresponding accelerometers (see Eq. (11)). Given that the four tri-axial accelerometers are in the same plane normal to the  $\vec{z}$  axis, then  $(z_i - z_j)$  is nil for any  $(i, j)$ . Thus, it is clear that, when  $[T]$  has two rows with a sensor direction in  $(\vec{x}, \vec{x})$ ,  $(\vec{y}, \vec{y})$  or  $(\vec{x}, \vec{y})$ , it will not have full rank and thus not be invertible. It may have full rank for arbitrary values during motion but the condition number will remain relatively high. Therefore, in this specific planar configuration, at least and only two of the three rows required must be related to a sensor direction in  $\vec{z}$ . Hence, from the initial 84 possible combinations of three subtractions, only 12 fulfill this condition. They are shown in Table 5 with their respective condition number of  $[T]$  without motion. It can be seen that they are of the same order and all reasonably low. Furthermore, 4 combinations have the minimum possible condition number of 1, whereas for the 8 others it is 2.618. This is due to the fact that for the latter, one subtraction of two non-neighboring sensors is used in  $\vec{z}$  (the subtraction number 6 associated to sensor T1 and T3 here), which makes the tangent matrix more complex. Hence, combination 2 of Table 5 was chosen in the experimental validation since it is one of four that provides the best condition number, at least at rest and thus irrespective of the test or the quality of the sensors measurements.

In contrast, depending on the motion to be characterized and the quality and position of the sensors, one of these 12 combinations can turn out to be optimal. It will no longer be found by assessing the condition number which, although varying with time, remains of the same order regardless of the motion. This choice will be based more on the accuracy with which the motion is predicted. Regarding the previous numerical/experimental comparisons of Sections 3.2 and 3.3, any other combination of Table 5 gives relatively similar results, since all the tri-axial accelerometers are from the same model (thus with same experimental bias), symmetrically positioned and the displacements remain small. This means that a quite arbitrary configuration of the sensor locations and directions can be used.

For the case of large rotations in Section 3.4, it appears that combinations 4, 5, 6, 7, 10 and 11 are unstable, owing to a divergent prediction of  $\alpha_2$ . The common feature of these combinations is to be composed with one accelerogram subtraction from two non-neighboring sensors T1 and T3 either in  $\vec{x}$  or  $\vec{y}$ . Thus, this accelerogram subtraction, which is normally only sensitive to the rotation of angle  $\alpha_2$ , is also sensitive to the rotation of angle  $\alpha_1$  due to their simultaneity and the coordinates of T1 and T3, creating uncertainty. In contrast, all these unstable combinations become stable and the results are satisfactory as soon as the motion is composed only of the rotation of angle  $\alpha_2$ . This shows that, for large combined rotations at least, it is preferable to set up the sensors so that each pair monitors only one rotation. Whatever the case, it will be expedient first to numerically simulate the motion under test and solve the inverse problem as done in Section 3.4 to state whether the location of the sensors is suitable (i.e. with stable and accurate results), before fixing the accelerometers onto the 6-DOF shaker.

Combination number	Subtraction combination	Accelerograms subtractions	Initial cond. number
1	(1,3,6)	(T1x-T2x,T1z-T2z,T1z-T3z)	2.618
2	(1,3,9)	(T1x-T2x,T1z-T2z,T1z-T4z)	1
3	(1,6,9)	(T1x-T2x,T1z-T3z,T1z-T4z)	2.618
4	(3,4,6)	(T1z-T2z,T1x-T3x,T1z-T3z)	2.618
5	(3,4,9)	(T1z-T2z,T1x-T3x,T1z-T4z)	1
6	(3,5,6)	(T1z-T2z,T1y-T3y,T1z-T3z)	2.618
7	(3,5,9)	(T1z-T2z,T1y-T3y,T1z-T4z)	1
8	(3,6,8)	(T1z-T2z,T1z-T3z,T1y-T4y)	2.618
9	(3,8,9)	(T1z-T2z,T1y-T4y,T1z-T4z)	1
10	(4,6,9)	(T1x-T3x,T1z-T3z,T1z-T4z)	2.618
11	(5,6,9)	(T1y-T3y,T1z-T3z,T1z-T4z)	2.618
12	(6,8,9)	(T1z-T3z,T1y-T4y,T1z-T4z)	2.618

Table 5: Suitable combinations of three subtractions of Table 4 for the rotation problem

## 5. DISCUSSION

The slight discrepancies between the results of the REDEAT method and the experimental ones can originate from several sources of error. Firstly, the sensors considered as a reference for the comparison may be biased or have a poorer quality than expected. This is for instance the case of the gyroscopes used in Section 3.2 and 3.3 that present noise as well as aliasing issues due to low sampling frequency. Likewise, some errors can be assigned to the inherent imperfections associated with the accelerometers used as inputs of the inverse problem, such as noise, uncertainty on positioning and orientation, calibration bias, etc. If only six accelerograms are used, then the problem is perfectly determined and there will always be a solution despite the errors in these inputs. In order to locate and quantify the source of error, there is no choice but to resort to additional accelerograms and solve the problem for different input configurations. Furthermore, if the sensors present high cross-sensitivity, the latter can eventually be accounted for in the inverse problem algorithm to limit error propagation. Running some simulated cases as that in Section 3.4 can also help to understand the deviation of the solutions when introducing some known defects in the fictitious accelerometers, such as calibration bias in amplitude or in phase.

Secondly, there are deviations related to the definition of the three parameters  $(f_c, t_0, t_1)$  of the REDEAT method. As seen in Section 4.1, a compromise may be made between accuracy and computational time consumption. Overall, the main discrepancies between the experimental results and those of the REDEAT method reside in low frequency, where the divergence related to double integration has the greatest effect. This can be troublesome for motion in this specific

range, but possibly irrelevant for a random excitation with a spectral content such as that in Section 3.3. Moreover and as expected, this mainly concerns the sensors subject to the lowest acceleration levels (e.g. sensor M3 in Fig. 12).

Finally, the remaining discrepancies may be tracked to the choice of the sensor locations and orientations. In particular, this can significantly affect the condition number of the matrix to be inverted in the inverse problem. The further this number is from one, the higher the number of numerical errors added to the experimental errors previously mentioned. It is therefore essential to reduce this as much as possible, at least in the static state, as detailed in Section 4.2.

## 6. CONCLUSION

An original approach combining numerical integration and data processing was proposed to determine the real displacements of multi-axial excitation shakers. This is of particular relevance to obtaining the real time variation of the 6 DOFs that must be used as inputs in any case of numerical/experimental comparison of an on-board structure. Moreover, it helps to quantify the error between a targeted motion required for a given test and the real motion reproduced by the device. As shown by the different tests that were carried out, the REDEAT method gives relatively accurate results, either for harmonic or random motion, and small or large displacements, with low computational cost. The three parameters  $f_c$ ,  $t_0$  and  $t_1$  were adjusted to enhance the predictions of the REDEAT method. Likewise, the position and orientation of the sensors played an important role. It was shown in the present paper that only six accelerograms are necessary, obtained from sensors located in the same plane. Although this technique was successfully applied to a 6-DOF shaker, it is clear that it can also work for systems with fewer degrees of freedom such as tri-axial tables.

One of the limits of the REDEAT method is the difficulty of using it for tests with very low spectral contents, in which case a delicate compromise must be found between removing the divergence issue from the algorithm while not filtering the minimum frequency of the test. Another drawback is that the REDEAT method works only when the initial conditions are known. In this sense, it is relatively well adapted when the measurements are started before the shaker begins moving, but of little use when recording starts during the motion. Furthermore, the numerical integration involves post-processing time cost that may prevent its suitability for real-time applications.

## Declaration of Competing Interest

None.

## Acknowledgements

This work was supported by the French National Research Agency (ANR) in the framework of the ANR-Labcom-SME AdViTAM, 16-LCV1-0006, and of Equipex PHARE 10-EQPX-0043.

## References

- [1] G.-F. Guan, H.-T. Wang, W. Xiong, Multi-input multi-output random vibration control of a multi-axis electro-hydraulic shaking table, *Journal of Vibration and Control* 21 (16) (2015) 3292–3304.
- [2] U. Musella, G. D’Elia, A. Carrella, B. Peeters, E. Mucchi, F. Marulo, P. Guillaume, A minimum drives automatic target definition procedure for multi-axis random control testing, *Mechanical Systems and Signal Processing* 107 (2018) 452–468.
- [3] R. Zheng, H. Chen, D. Vandepitte, S. Gallas, B. Zhang, Generation of sine on random vibrations for multi-axial fatigue tests, *Mechanical Systems and Signal Processing* 126 (2019) 649–661.
- [4] G. D’Elia, U. Musella, E. Mucchi, P. Guillaume, B. Peeters, Analyses of drives power reduction techniques for multi-axis random vibration control tests, *Mechanical Systems and Signal Processing* 135 (2020) 106395.
- [5] K. Kersch, A. Schmidt, E. Woschke, Multiaxial fatigue damage evaluation: A new method based on modal velocities, *Journal of Sound and Vibration* (2020) 115297.
- [6] Z. Geng, L. S. Haynes, Six-degree-of-freedom active vibration isolation using a stewart platform mechanism, *Journal of Robotic Systems* 10 (5) (1993) 725–744.

- [7] B. Dasgupta, T. Mruthyunjaya, The stewart platform manipulator: a review, *Mechanism and machine theory* 35 (1) (2000) 15–40.
- [8] M. A. Underwood, T. Keller, Applying coordinate transformations to multi-dof shaker control, *Sound and Vibration* 40 (1) (2006) 14–27.
- [9] R. Zheng, H. Chen, D. Vandepitte, Z. Luo, Multi-exciter stationary non-gaussian random vibration test with time domain randomization, *Mechanical Systems and Signal Processing* 122 (2019) 103–116.
- [10] Z. Luo, H. Chen, R. Zheng, W. Zheng, A damage gradient model for fatigue life prediction of notched metallic structures under multiaxial random vibrations, *Fatigue & Fracture of Engineering Materials & Structures* 43 (9) (2020) 2101–2115.
- [11] K. Kersch, E. Woschke, Fixture modifications for effective control of an electrodynamic 3d-shaker system, *Sound & Vibration* 54 (2) (2020) 75–84.
- [12] F. De Coninck, W. Desmet, P. Sas, Increasing the accuracy of mdof road reproduction experiments: Calibration, tuning and a modified twr approach, in: *Proceedings of ISMA*, Citeseer, 2004, pp. 19–22.
- [13] P. Hu, B. Chen, C. Zhang, Q. Wu, Correlation-averaging methods and kalman filter based parameter identification for a rotational inertial navigation system, *IEEE Transactions on Industrial Informatics* 15 (3) (2018) 1321–1328.
- [14] I. Skog, J.-O. Nilsson, P. Händel, A. Nehorai, Inertial sensor arrays, maximum likelihood, and cramér–rao bound, *IEEE Transactions on Signal Processing* 64 (16) (2016) 4218–4227.
- [15] J.-O. Nilsson, I. Skog, Inertial sensor arrays - a literature review, in: *2016 European Navigation Conference (ENC)*, IEEE, 2016, pp. 1–10.
- [16] D. Wang, G. Yuan, A six-degree-of-freedom acceleration sensing method based on six coplanar single-axis accelerometers, *IEEE Transactions on Instrumentation and Measurement* 60 (4) (2010) 1433–1442.
- [17] Z. Luo, C. Liu, S. Yu, S. Zhang, S. Liu, Design and analysis of a novel virtual gyroscope with multi-gyroscope and accelerometer array, *Review of Scientific Instruments* 87 (8) (2016) 085003.
- [18] A. R. Schuler, A. Grammatikos, K. A. Fegley, Measuring rotational motion with linear accelerometers, *IEEE transactions on aerospace and electronic systems AES-3* (3) (1967) 465–472.
- [19] A. J. Padgaonkar, K. Krieger, A. King, Measurement of angular acceleration of a rigid body using linear accelerometers, *Journal of Applied Mechanics* 42 (3) (1975) 552–556.
- [20] P. Cardou, G. Fournier, P. Gagnon, A nonlinear program for angular-velocity estimation from centripetal-acceleration measurements, *IEEE/ASME Transactions on Mechatronics* 16 (5) (2010) 932–944.
- [21] P. Schopp, L. Klingbeil, C. Peters, Y. Manoli, Design, geometry evaluation, and calibration of a gyroscope-free inertial measurement unit, *Sensors and Actuators A: Physical* 162 (2) (2010) 379–387.
- [22] S. O. Madgwick, A. J. Harrison, P. M. Sharkey, R. Vaidyanathan, W. S. Harwin, Measuring motion with kinematically redundant accelerometer arrays: Theory, simulation and implementation, *Mechatronics* 23 (5) (2013) 518–529.
- [23] E. Edwan, S. Knedlik, O. Loffeld, Angular motion estimation using dynamic models in a gyro-free inertial measurement unit, *Sensors* 12 (5) (2012) 5310–5327.
- [24] T. Zou, F. Ni, C. Guo, K. Li, H. Liu, A 6-dof acceleration sensor with cylindrical configuration, *Sensors and Actuators A: Physical* 251 (2016) 167–178.
- [25] D. Giansanti, V. Macellari, G. Maccioni, A. Cappozzo, Is it feasible to reconstruct body segment 3-d position and orientation using accelerometric data?, *IEEE transactions on biomedical engineering* 50 (4) (2003) 476–483.
- [26] R. Onodera, N. Mimura, 6-dof motion sensor system using multiple linear accelerometers, in: *Humanoid Robots*, IntechOpen, 2009.
- [27] M. Miles, Measurement of six-degree of freedom model motions using strapdown accelerometers, in: *21st American Towing Tank Conference*, 1986, pp. 369–375.
- [28] K.-J. Bathe, *Finite element procedures*, Klaus-Jurgen Bathe, 2006.